ELSEVIER

Mechanics of Materials 32 (2000) 561–591

MECHANICS OF MATERIALS

www.elsevier.com/locate/mechmat

Interfacial debonding analysis in multiple fiber reinforced composites

Somnath Ghosh [a,*], Yong Ling [a], Bhaskar Majumdar [b], Ran Kim [c]

[a] *Department of Mechanical Engineering, The Ohio State University, 206 West 18th Avenue, Columbus, OH 43210-1154, USA*
[b] *Department of Materials Science and Engineering, New Mexico Institute of Technology, NM, USA*
[c] *University of Dayton Research Institute, Dayton, OH, USA*

Received 28 February 2000; received in revised form 6 June 2000

Abstract

Decohesion at multiple fiber interfaces of elastic fiber reinforced composites is modeled by the Voronoi cell finite element model (VCFEM) in this paper. Interfacial debonding is accommodated by cohesive zone models, in which normal and tangential springs tractions are expressed in terms of interfacial separation. Model simulations are compared with results from experiments using cruciform specimens, of single and multiple fiber polymer-matrix composites. An inverse problem is solved to calibrate the cohesive zone parameters. Debonding at fiber-matrix interfaces is simulated for different architectures, volume fractions and boundary conditions, to understand the influence of microstructural morphology and boundary conditions on the decohesion process.

Keywords: Interfacial debonding; Cohesive zone; Voronoi cell FEM; Multiple fiber composites

1. Introduction

Affordability issues are gradually shifting design practice away from the assembly of small sub-components towards large unitized structures. In this paradigm shift, greater emphasis is placed on design based on analysis, rather than on laboratory tests. The micro-mechanisms of failure in composite materials, e.g. polymer or organic matrix composites are generally known. They involve either fiber splitting or fiber-matrix interface decohesion, followed by matrix cracking. The damage mechanisms are sensitive to local morphological parameters like volume fraction, size, shape and spatial distribution of reinforcements, interfacial strength and process-related defects. Fibers and interfaces, in regions of clustering or preferential alignment, are subjected to increased local stresses and have a greater propensity to undergo damage nucleation than those in dilute regions. A number of failure prediction models for composite laminates are phenomenological and have been based on empirical methods or ply level fracture mechanics. These macroscopic models are not capable of relating the failure process to local interactions and stress

* Corresponding author. Tel.: +1-614-292-2599; fax: +1-614-292-7369.
E-mail address: ghosh.5@osu.edu (S. Ghosh).

0167-6636/00/$ - see front matter
PII: S0167-6636(00)00030-2

concentrations. Because of limited large-scale tests in the emerging design environment, it is critical that a robust failure analysis model evolves from details of the microstructure and incorporates the micromechanics of damage modes.

Analysis of damage evolution by decohesion of fiber-matrix interfaces in multiple fiber reinforced microstructures is the objective of the present study. The effect of weak bonding or debonded interface on the mechanical properties has been studied by several investigators (e.g. Benveniste, 1984; Hashin, 1990; Pagano and Tandon, 1990), using simplified models for representing imperfect conditions through traction discontinuities. The propagation of interfacial cracking or decohesion at fiber-matrix interfaces has been successfully modeled by a number of researchers using the cohesive volumetric finite element methods. Among the important contributions to the field of damage evolution by normal and tangential separation are those by Needleman (1987, 1990, 1992), Tvegaard (1995, 1990), Allen et al. (1994), Lo and Allen (1994), Lissenden (1990), Geubelle (1995, in press) and Walter et al. (1997). A majority of these studies have used unit cell models, which assume that the material is constituted of periodic repetition of single cells. Displacement based finite element analyses, with the inclusion-matrix interface represented through traction-displacement constitutive models, are used to predict the onset and growth of debonding. While these models provide valuable insights into the microstructural damage processes, the simple microstructure are ineffective in addressing the interaction between fibers, effects of clustering, alignment, relative sizes, etc. that are often observed in micrographs. To overcome this limitation, Zhong and Knauss (1997) have proposed a hybrid discrete-continuum approach in which discrete particle interactions with damage evolution are modeled, accounting for particle size and spacing.

In this paper, decohesion at multiple fiber interfaces is modeled for polymer matrix composites by the Voronoi cell finite element model (VCFEM), developed by Moorthy and Ghosh (1996). VCFEM has been established as an effective tool for efficient and accurate modeling of non-uniform microstructures with heterogeneities of arbitrary shapes, sizes or dispersions with perfect interfaces in Ghosh and Moorthy (1995), and Moorthy and Ghosh (1996, 2000). In VCFEM, the computational model evolves by tessellation of the microstructure to generate a mesh of multi-sided Voronoi polygons as shown in Fig. 1. The Voronoi cell formulation is advanced in this paper to incorporate interfacial debonding by introducing cohesive zone models. This is accomplished by permitting the elastic matrix and inclusion phases to be connected at nodes by normal and tangential cohesive springs. The debonding process is assumed to be quasi-static, neglecting inertia. The analysis is assumed to be in-plane and post-debonding friction is neglected in this study. Simulations with the model are compared with results from experiments performed using single and multiple

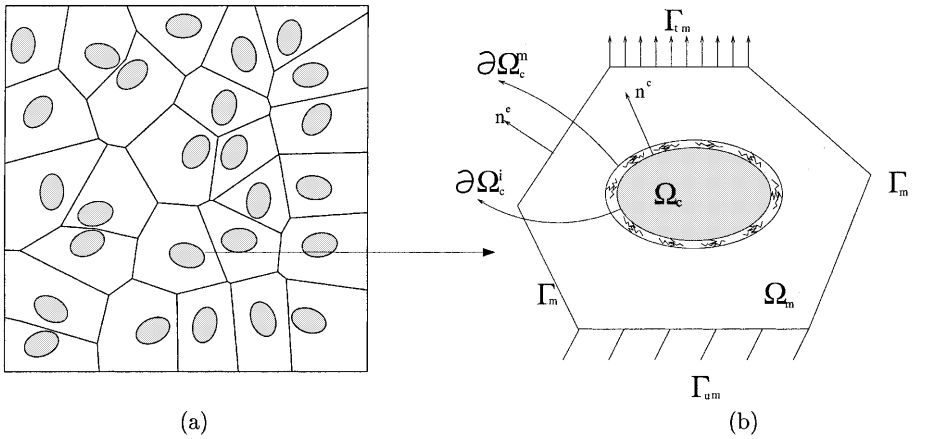

Fig. 1. (a) A mesh of Voronoi cell elements generated by tessellation of the heterogeneous microstructural domain. (b) A typical Voronoi cell element with delineation of the phases and interface region.

fiber cruciform specimens. An inverse problem is solved, using minimization techniques to calibrate cohesive zone parameters for comparison studies. Finally, debonding at multi-fiber interfaces is simulated for different architectures, volume fractions and boundary conditions to understand their effect on decohesion.

2. Interfacial debonding with the Voronoi cell FEM

The VCFEM for a heterogeneous domain with a dispersion of inclusions or voids, implements a mesh of Voronoi polytopes. The Voronoi cells, surrounding each heterogeneity, are generated by a surface based tessellation algorithm (Ghosh and Mukhopadhyay, 1991; Li et al., 1999) to yield multiple edges depending on the number of neighboring heterogeneities. Each element in VCFEM consists of the heterogeneity and its neighborhood region of matrix. No further refinement of the element is required. VCFEM has been successfully developed by Ghosh and Moorthy (1995, 1996, 2000) for accurate stress and deformation analysis of elastic and plastic materials with perfect interfaces. It uses an assumed stress hybrid finite element formulation (Ghosh and Moorthy, 1995, 2000) with specially developed equilibriated stress fields, consistent with micromechanics. VCFEM is able to significantly enhance computing efficiency for complex microstructures compared to conventional displacement based FEM packages. Large regions of the microstructure are thereby easily modeled by this method. A brief account of VCFEM to model inclusion-matrix interfacial debonding is presented next.

Consider a typical multiphase domain or representative volume element Ω consisting of N inclusions (see Fig. 1(a)), each contained in a Voronoi cell element Ω_e, as shown in Fig. 1(b). The matrix and the inclusion or reinforcement phases in each element are denoted by Ω_m and Ω_c, respectively, i.e., $\Omega_e = \Omega_m \cup \Omega_c$. Each element boundary $\partial\Omega_e$ is assumed to be composed of the prescribed traction and displacement boundaries Γ_{tm} and Γ_{um}, respectively, and the inter-element boundary Γ_m, i.e., $\partial\Omega_e = \Gamma_{tm} \cup \Gamma_{um} \cup \Gamma_m$. For allowing decohesion of the matrix–inclusion interface, an incompatible displacement field is facilitated across the interface through a set of connected node-pairs. The nodes in each pair belong to the matrix and inclusion boundaries $\partial\Omega_c^m$ and $\partial\Omega_c^c$, respectively. $\partial\Omega_c^c$ has an outward normal $\mathbf{n}^c$ $(= \mathbf{n}^m)$, while $\mathbf{n}^e$ is the outward normal to $\partial\Omega_e$. It should be noted that the interfacial zone has zero thickness prior to deformation, but nodes may separate with progression of deformation and onset of decohesion.

An incremental VCFEM formulation accommodates evolving interfacial damage with changing applied loads, deformation and stress fields. Let $\boldsymbol{\sigma}^m$ and $\boldsymbol{\sigma}^c$ be the equilibriated stress fields and $\boldsymbol{\epsilon}^m$ and $\boldsymbol{\epsilon}^c$ the corresponding strain fields in the matrix and inclusion phases of each Voronoi element respectively. The prefix Δ corresponds to increments. Furthermore, let $\mathbf{u}$, $\mathbf{u}^m$ and $\mathbf{u}^c$ denote kinematically admissible displacement fields on $\partial\Omega_e$, $\partial\Omega_c^m$ and $\partial\Omega_c^c$, respectively. A complementary energy functional may be expressed for each element in terms of increments of stress and boundary/interface displacement fields as

$$
\begin{aligned}
\Pi_e(\boldsymbol{\sigma}, \Delta\boldsymbol{\sigma}, \mathbf{u}, \Delta\mathbf{u}) = & -\int_{\Omega_m} \Delta B(\boldsymbol{\sigma}^m, \Delta\boldsymbol{\sigma}^m)\,\mathrm{d}\Omega - \int_{\Omega_c} \Delta B(\boldsymbol{\sigma}^c, \Delta\boldsymbol{\sigma}^c)\,\mathrm{d}\Omega - \int_{\Omega_m} \boldsymbol{\epsilon}^m :\ \Delta\boldsymbol{\sigma}^m\,\mathrm{d}\Omega \\
& - \int_{\Omega_c} \boldsymbol{\epsilon}^c :\ \Delta\boldsymbol{\sigma}^c\,\mathrm{d}\Omega + \int_{\partial\Omega_e} (\boldsymbol{\sigma}^m + \Delta\boldsymbol{\sigma}^m)\cdot\mathbf{n}^e\cdot(\mathbf{u}^m + \Delta\mathbf{u}^m)\,\mathrm{d}\partial\Omega \\
& - \int_{\Gamma_{tm}} (\bar{\mathbf{t}} + \Delta\bar{\mathbf{t}})\cdot(\mathbf{u}^m + \Delta\mathbf{u}^m)\,\mathrm{d}\Gamma - \int_{\partial\Omega_c^m} (\boldsymbol{\sigma}^m + \Delta\boldsymbol{\sigma}^m)\cdot\mathbf{n}^c\cdot(\mathbf{u}^m + \Delta\mathbf{u}^m)\,\mathrm{d}\partial\Omega \\
& + \int_{\partial\Omega_c^c} (\boldsymbol{\sigma}^c + \Delta\boldsymbol{\sigma}^c)\cdot\mathbf{n}^c\cdot(\mathbf{u}^c + \Delta\mathbf{u}^c)\mathrm{d}\partial\Omega - \int_{\partial\Omega_m^c/\partial\Omega_c^c} \int_{(u_n^m - u_n^c)}^{(u_n^m + \Delta u_n^m - u_n^c - \Delta u_n^c)} T_n^m\,\mathrm{d}(u_n^m - u_n^c)\,\mathrm{d}\partial\Omega \\
& - \int_{\partial\Omega_m^c/\partial\Omega_c^c} \int_{(u_t^m - u_t^c)}^{(u_t^m + \Delta u_t^m - u_t^c - \Delta u_t^c)} T_t^m\,\mathrm{d}(u_t^m - u_t^c)\,\mathrm{d}\partial\Omega, \qquad (1)
\end{aligned}
$$

where B is the complementary energy density and the superscripts m and c correspond to variables associated with the matrix and inclusion phases. The different terms in the right-hand side of Eq. (1) are included to provide weak forms of essential governing equations of the problem. The fifth term corresponds to inter-element traction reciprocity while the sixth term accounts for the boundary traction. The last two terms provide the work done by the interfacial tractions $\mathbf{T}^{\mathrm{m}} = T_{\mathrm{n}}^{\mathrm{m}}\mathbf{n}^{\mathrm{m}} + T_{\mathrm{t}}^{\mathrm{m}}\mathbf{t}^{\mathrm{m}}$ due to interfacial separation $(\mathbf{u}^{\mathrm{m}} - \mathbf{u}^{\mathrm{c}})$, where T_{n} and T_{t} are the normal and tangential components. The traction on the matrix interface $\partial\Omega_{\mathrm{m}}^{\mathrm{c}}$ is related to the stresses and interface normals as

$$\mathbf{T}^{\mathrm{m}} = \boldsymbol{\sigma}^{\mathrm{m}} \cdot \mathbf{n}^{\mathrm{m}} = -\boldsymbol{\sigma}^{\mathrm{m}} \cdot \mathbf{n}^{\mathrm{c}} = -\boldsymbol{\sigma}^{\mathrm{c}} \cdot \mathbf{n}^{\mathrm{c}}. \tag{2}$$

The interfacial response is described by constitutive relations that prescribe the dependence of interface tractions on interfacial separation. The total energy for the entire heterogeneous domain is obtained by adding the energy functionals for N elements

$$\Pi = \sum_{e=1}^{N} \Pi_{\mathrm{e}}. \tag{3}$$

Equating the variation of Π_{e} in Eq. (2) with respect to stress increments $\Delta\boldsymbol{\sigma}^{\mathrm{m}}$ and $\Delta\boldsymbol{\sigma}^{\mathrm{c}}$ to zero, yields the element displacement compatibility relations in each of the phases Ω_{m} and Ω_{c}. Furthermore, setting the variation of Π in Eq. (3) with respect to the independent boundary displacements $\Delta\mathbf{u}$, $\Delta\mathbf{u}^{\mathrm{m}}$ and $\Delta\mathbf{u}^{\mathrm{c}}$ to zero, yields the traction reciprocity conditions on the interelement boundaries (Γ_{m}) and traction boundaries (Γ_{tm}), and fiber–matrix interfaces, $\partial\Omega_{\mathrm{c}}^{\mathrm{m}}$ and $\partial\Omega_{\mathrm{c}}^{\mathrm{c}}$, respectively.

2.1. Hybrid element assumptions and weak forms

Independent assumptions on stress increments $\Delta\boldsymbol{\sigma}$ are made in the matrix and inclusion phases to accommodate stress jumps across the interface. In two-dimensional analysis, Airy's stress function $\boldsymbol{\Phi}(x, y)$ is a convenient tool for deriving equilibriated stress-increments. Important micromechanics observations, that interfacial stress concentrations depend on the shape of the inclusion have been incorporated in the choice of stress functions, by Moorthy and Ghosh (1996) through the decomposition of the matrix stress functions into (a) a purely polynomial function $\boldsymbol{\Phi}_{\mathrm{poly}}^{\mathrm{m}}$ and (b) a reciprocal function $\boldsymbol{\Phi}_{\mathrm{rec}}^{\mathrm{m}}$ ($\boldsymbol{\Phi}^{\mathrm{m}} = \boldsymbol{\Phi}_{\mathrm{poly}}^{\mathrm{m}} + \boldsymbol{\Phi}_{\mathrm{rec}}^{\mathrm{m}}$). The inclusion stress functions are admitted as polynomial function $\boldsymbol{\Phi}_{\mathrm{poly}}^{\mathrm{c}}(\boldsymbol{\Phi}^{\mathrm{c}} = \boldsymbol{\Phi}_{\mathrm{poly}}^{\mathrm{c}})$. The pure polynomial function $\boldsymbol{\Phi}_{\mathrm{poly}}$ accommodates the far field stress in the matrix and inclusion and are written as

$$\boldsymbol{\Phi}_{\mathrm{poly}}^{\mathrm{m}} = \sum_{p,q} \xi^p \eta^q \Delta\beta_{pq}^{\mathrm{m}}, \quad \boldsymbol{\Phi}_{\mathrm{poly}}^{\mathrm{c}} = \sum_{p,q} \xi^p \eta^q \Delta\beta_{pq}^{\mathrm{c}}, \tag{4}$$

where (ξ, η) correspond to scaled local coordinates with origin at the element centroid $(x_{\mathrm{c}}, y_{\mathrm{c}})$, written as

$$\xi = (x - x_{\mathrm{c}})/L, \quad \eta = (y - y_{\mathrm{c}})/L \tag{5}$$

and the scale parameter $L = \sqrt{\max(x - x_{\mathrm{c}}) \times \max(y - y_{\mathrm{c}})}$ $\forall (x, y) \in \partial\Omega_{\mathrm{e}}$. The scaling to (ξ, η) leads to an approximate range of variation $-1 \leqslant \xi \leqslant 1$ and $-1 \leqslant \eta \leqslant 1$ in most Voronoi cell elements. Note that this range is exactly true for square elements. The use of the local coordinates (ξ, η) instead of global coordinates (x, y) prevents numerical inaccuracies due to high exponents of (x, y) in $\boldsymbol{\Phi}^{\mathrm{m}}$ and $\boldsymbol{\Phi}^{\mathrm{c}}$, and thus prevent ill-conditioning of the element stiffness matrices. Two considerations dominate the choice of the reciprocal stress function in the matrix $\boldsymbol{\Phi}_{\mathrm{rec}}^{\mathrm{m}}$. They are: (a) the function must facilitate stress concentration near the interface, strongly accounting for the inclusion or void shape, and decay at large distances from it, and (b) the interfacial traction field in the matrix should provide for a matching traction field in the inclusion for composite materials or reduce to zero for porous materials. Consequently, the function $\boldsymbol{\Phi}_{\mathrm{rec}}^{\mathrm{m}}$ is constructed from the inverse of a mapped radial coordinate f as

$$\mathbf{\Phi}^{\mathrm{m}}_{\mathrm{rec}} = \sum_{p,q} \xi^p \eta^q \sum_{i=1}^{n} \frac{1}{f^{p+q+i-1}} \Delta\beta^{\mathrm{m}}_{pqi} = \sum_{p,q} \xi^p \eta^q \left(\frac{\Delta\beta^{\mathrm{m}}_{pq1}}{f^{p+q}} + \frac{\Delta\beta^{\mathrm{m}}_{pq2}}{f^{p+q+1}} + \cdots \right). \tag{6}$$

In 2D, f can be generated by Schwarz–Christoffel conformal transformation of an elliptical interface $\partial\Omega_{\mathrm{c}}$ (Muskhelishvili, 1961), or by a Fourier series transformation for arbitrary shapes such as squares (see Moorthy and Ghosh, 1996), whereas in 3D, ellipsoidal coordinates may be chosen to represent f. The mapped radial coordinate f has the properties

$$f(x,y) = 1 \quad \text{on } \partial\Omega^{\mathrm{m}}_{\mathrm{c}} \quad \text{and} \quad \frac{1}{f(x,y)} \to 0 \quad \text{as } (x,y) \to \infty. \tag{7}$$

Stress increments in the matrix and inclusion phases of Voronoi cell elements are obtained by differentiating the stress functions $\mathbf{\Phi}^{\mathrm{m}}$ and $\mathbf{\Phi}^{\mathrm{c}}$ to yield:

$$\begin{Bmatrix} \Delta\sigma^{\mathrm{m}}_{xx} \\ \Delta\sigma^{\mathrm{m}}_{yy} \\ \Delta\sigma^{\mathrm{m}}_{xy} \end{Bmatrix} = \begin{Bmatrix} \frac{1}{L^2}\frac{\partial^2}{\partial\eta^2}\left(\sum_{p,q} \xi^p \eta^q \Delta\beta^{\mathrm{m}}_{pq} + \sum_{p,q} \xi^p \eta^q \sum_{i=1}^{n} \frac{1}{f^{p+q+i-1}} \Delta\beta^{\mathrm{m}}_{pqi} \right) \\ \frac{1}{L^2}\frac{\partial^2}{\partial\xi^2}\left(\sum_{p,q} \xi^p \eta^q \Delta\beta^{\mathrm{m}}_{pq} + \sum_{p,q} \xi^p \eta^q \sum_{i=1}^{n} \frac{1}{f^{p+q+i-1}} \Delta\beta^{\mathrm{m}}_{pqi} \right) \\ -\frac{1}{L^2}\frac{\partial^2}{\partial\xi\partial\eta}\left(\sum_{p,q} \xi^p \eta^q \Delta\beta^{\mathrm{m}}_{pq} + \sum_{p,q} \xi^p \eta^q \sum_{i=1}^{n} \frac{1}{f^{p+q+i-1}} \Delta\beta^{\mathrm{m}}_{pqi} \right) \end{Bmatrix}$$

$$= [\mathbf{P}^{\mathrm{m}}_{\mathrm{poly}}] \begin{Bmatrix} \Delta\beta^{\mathrm{m}}_{11} \\ \vdots \\ \Delta\beta^{\mathrm{m}}_{pq} \\ \vdots \end{Bmatrix} + [\mathbf{P}^{\mathrm{m}}_{\mathrm{rec}}] \begin{Bmatrix} \Delta\beta^{\mathrm{m}}_{111} \\ \vdots \\ \Delta\beta^{\mathrm{m}}_{pqi} \\ \vdots \end{Bmatrix} = [\mathbf{P}^{\mathrm{m}}]\{\Delta\boldsymbol{\beta}^{\mathrm{m}}\} \tag{8}$$

and

$$\begin{Bmatrix} \Delta\sigma^{\mathrm{c}}_{xx} \\ \Delta\sigma^{\mathrm{c}}_{yy} \\ \Delta\sigma^{\mathrm{c}}_{xy} \end{Bmatrix} = \begin{Bmatrix} \frac{1}{L^2}\frac{\partial^2}{\partial\eta^2}\left(\sum_{p,q} \xi^p \eta^q \Delta\beta^{\mathrm{c}}_{pq} \right) \\ \frac{1}{L^2}\frac{\partial^2}{\partial\xi^2}\left(\sum_{p,q} \xi^p \eta^q \Delta\beta^{\mathrm{c}}_{pq} \right) \\ -\frac{1}{L^2}\frac{\partial^2}{\partial\xi\partial\eta}\left(\sum_{p,q} \xi^p \eta^q \Delta\beta^{\mathrm{c}}_{pq} \right) \end{Bmatrix} = [\mathbf{P}^{\mathrm{c}}]\{\Delta\boldsymbol{\beta}^{\mathrm{c}}\}. \tag{9}$$

Coefficients $\Delta\beta^{\mathrm{m}}_{pqi}$ in Eq. (8) add flexibility to polynomial coefficients $\Delta\beta^{\mathrm{m}}_{pq}$ in the stress expansions for matching desired tractions at the interface ($f = 1$) and the gradient of f accounts for the shape of the interface. Terms produced by the reciprocal function have negligible effects on the traction vectors far away from the heterogeneity, and these are produced predominantly by polynomial terms in the stress function.

Compatible displacement increments are generated by interpolation in terms of nodal displacements on $\partial\Omega_{\mathrm{e}}$, $\partial\Omega^{\mathrm{m}}_{\mathrm{c}}$ and $\partial\Omega^{\mathrm{c}}_{\mathrm{c}}$ using conventional linear or quadratic shape functions

$$\begin{aligned} &\{\Delta\mathbf{u}\} = [\mathbf{L}^{\mathrm{e}}]\{\Delta\mathbf{q}\} \quad \text{on } \partial\Omega_{\mathrm{e}}, \quad \{\Delta\mathbf{u}^{\mathrm{m}}\} = [\mathbf{L}^{\mathrm{c}}]\{\Delta\mathbf{q}^{\mathrm{m}}\} \quad \text{on } \partial\Omega^{\mathrm{m}}_{\mathrm{c}}, \\ &\{\Delta\mathbf{u}^{\mathrm{c}}\} = [\mathbf{L}^{\mathrm{c}}]\{\Delta\mathbf{q}^{\mathrm{c}}\} \quad \text{on } \partial\Omega^{\mathrm{c}}_{\mathrm{c}}, \end{aligned} \tag{10}$$

where $\{\Delta\mathbf{q}\}$, $\{\Delta\mathbf{q}^{\mathrm{m}}\}$ and $\{\Delta\mathbf{q}^{\mathrm{c}}\}$ are the generalized nodal displacement vectors on the element boundary and on the matrix and inclusion phases on the interface, respectively.

In general the interface displacements in the matrix $\{\Delta\mathbf{q}^{\mathrm{m}}\}$ are independent of the element boundary displacements $\{\Delta\mathbf{q}\}$. In order for the stiffness matrix to be non-singular, it is necessary to impose additional conditions that the element boundary and the interface have the same rigid body modes. These conditions are satisfied by equating rigid body modes on the interface to the rigid body modes on the element boundary. Consider the interface displacement field $\{\Delta\mathbf{q}^{\mathrm{m}}\}$ to be the sum of a rigid body mode and a purely deformation mode, expressed as

$$\{\Delta\mathbf{q}^{\mathrm{m}}\} = [\boldsymbol{\phi}]^{\mathrm{m}}\{\boldsymbol{\alpha}\}^{\mathrm{m}} + \{\Delta\mathbf{q}^{\mathrm{m}}\}^{\mathrm{def}}, \tag{11}$$

where $\{\Delta\mathbf{q}^{\mathrm{m}}\}^{\mathrm{def}}$ is the pure deformation part of $\{\Delta\mathbf{q}^{\mathrm{m}}\}$, $\{\boldsymbol{\alpha}^{\boldsymbol{m}}\}$ corresponds to the rigid body modes and $[\boldsymbol{\phi}]^{\mathrm{m}}$ is a rigid body displacement matrix in terms of interface coordinates $(x_i^{\mathrm{m}}, y_i^{\mathrm{m}})$. Since the pure deformation mode is orthogonal to the space spanned by rigid body modes, $\{\Delta\mathbf{q}^{\mathrm{m}}\}^{\mathrm{def}}$ lies in the null space of $[\boldsymbol{\phi}]^{\mathrm{m}}$. Equating the rigid body modes on the interface $\partial\Omega_{\mathrm{c}}^{\mathrm{m}}$ ($\{\boldsymbol{\alpha}^{\boldsymbol{m}}\}$) to the rigid body modes on the element boundary $\partial\Omega_{\mathrm{e}}(\{\boldsymbol{\alpha}^{e}\})$, results in a constraint equation for the displacements

$$\{[\boldsymbol{\phi}^{\mathrm{m}}]^{\mathrm{T}}[\boldsymbol{\phi}^{\mathrm{m}}]\}^{-1}[\boldsymbol{\phi}^{\mathrm{m}}]^{\mathrm{T}}\{\Delta\mathbf{q}^{\mathrm{m}}\} = \{[\boldsymbol{\phi}^{\mathrm{e}}]^{\mathrm{T}}[\boldsymbol{\phi}^{\mathrm{e}}]\}^{-1}[\boldsymbol{\phi}^{\mathrm{e}}]^{\mathrm{T}}\{\Delta\mathbf{q}^{\mathrm{e}}\} \quad \text{or} \quad [\hat{\boldsymbol{\Phi}}]\begin{Bmatrix} \Delta\mathbf{q} \\ \Delta\mathbf{q}^{\mathrm{m}} \end{Bmatrix} = \{\mathbf{0}\}. \tag{12}$$

This constraint needs to be imposed for making the element stiffness non-singular and invertible.

2.2. Cohesive zone models for interfacial decohesion

An alternative to the crack initiation and propagation criteria based on the evaluation of traditional fracture mechanics parameters K and J has been pioneered by Dugdale (1960), Barenblatt (1962), Rice (1968) and others. This approach uses cohesive zone interfacial models to depict fracture as a phenomenon of progressive separation across an extended crack tip or cohesive zone, that is resisted by cohesive tractions. Traction across the interface reaches a maximum, subsequently decreases and eventually vanishes with increasing interfacial separation, signaling complete decohesion. Dimensional considerations introduce a characteristic length in these models. The interface mechanical response is specified in terms of critical interfacial strength and work of separation per unit area and no additional failure criteria are required. A number of cohesive zone models have been developed to characterize interfacial decohesion at the continuum scale. Needleman (1987, 1990, 1992) has proposed a potential based framework to describe debonding initiation through complete separation in the cohesive zone. A similar potential based model has also been developed by Tvegaard (1995, 1990). Cohesive zone models utilizing nonlinear spring models to depict the interfacial failure process have been proposed by Ungsuwarungsri and Knauss (1987), Zhong and Knauss (1997), Geubelle (1995) and Lin et al. (in press). From thermodynamic considerations, Costanzo and Allen (1995), Costanzo and Walton (1997) have postulated rate dependent cohesive zone models with internal state variables to represent microscopic dissipation mechanisms. Camacho and Ortiz (1996), Ortiz and Pandolfi (1999) have developed a class of irreversible cohesive laws from potential or free energy functions for tracking dynamically growing cracks.

In this paper, the rate-independent cohesive zone models of Needleman (1987, 1990, 1992), Geubelle (1995) and Lin et al. (in press) are incorporated in the Voronoi cell FEM to model initiation and progressive debonding of matrix-inclusion interfaces in composites. The loading portion of the interfacial decohesion is manifested by these laws. In Needleman's model, the normal and tangential components of interfacial traction are derived from a potential, that is expressed in terms of polynomial or exponential functions of displacement jumps or separation across the interface. The potential using polynomial (cubic) functions is expressed in the form:

$$\phi(u_n,u_t)=\frac{27}{4}\sigma_{max}\delta^*\left\{\frac{1}{2}\left(\frac{u_n}{\delta^*}\right)^2\left[1-\frac{4}{3}\left(\frac{u_n}{\delta^*}\right)+\frac{1}{2}\left(\frac{u_n}{\delta^*}\right)^2\right]+\frac{1}{2}\alpha\left(\frac{u_t}{\delta^*}\right)^2\left[1-2\left(\frac{u_n}{\delta^*}\right)+\left(\frac{u_n}{\delta^*}\right)^2\right]\right\}\quad \forall u_n\leqslant\delta^*, \tag{13}$$

where u_n and u_t are the normal and tangential components of displacement jump at the interface. The cohesive zone parameters are σ_{max}, the maximum traction carried by the interface undergoing a purely normal separation, i.e., $u_t=0$, δ^*, a characteristic length and α, the ratio of interface shear to normal stiffness of the interface. The tractions are obtained by differentiating the potential as

$$\begin{aligned}T_n&=-\frac{\partial\phi}{\partial u_n}=-\frac{27}{4}\sigma_{max}\left\{\left(\frac{u_n}{\delta^*}\right)\left[1-2\left(\frac{u_n}{\delta^*}\right)+\left(\frac{u_n}{\delta^*}\right)^2\right]+\alpha\left(\frac{u_t}{\delta^*}\right)^2\left[\left(\frac{u_n}{\delta^*}\right)-1\right]\right\},\\ T_t&=-\frac{\partial\phi}{\partial u_t}=-\frac{27}{4}\sigma_{max}\left\{\alpha\left(\frac{u_t}{\delta^*}\right)\left[1-2\left(\frac{u_n}{\delta^*}\right)+\left(\frac{u_n}{\delta^*}\right)^2\right]\right\},\end{aligned} \tag{14}$$

For $u_n>\delta^*$, the traction components T_n and T_t are zero in this model. In an alternative form, the potential is expressed using exponential functions of the separation as

$$\phi(u_n,u_t)=\frac{9}{16}\sigma_{max}\delta^*\times\left\{1-\left[1+z\left(\frac{u_n}{\delta^*}\right)-\frac{1}{2}\alpha z^2\left(\frac{u_t}{\delta^*}\right)^2\right]e^{-z(u_n/\delta^*)}\right\}, \tag{15}$$

where $z=16e/9$. Thus the interfacial traction components are

$$\begin{aligned}T_n&=-\frac{\partial\phi}{\partial u_n}=-\sigma_{max}e\left\{z\left(\frac{u_n}{\delta^*}\right)-\frac{1}{2}\alpha z^2\left(\frac{u_t}{\delta^*}\right)^2\right\}e^{-z(u_n/\delta^*)},\\ T_t&=-\frac{\partial\phi}{\partial u_t}=-\sigma_{max}e\left\{\alpha z\left(\frac{u_n}{\delta^*}\right)\right\}e^{-z(u_n/\delta^*)}.\end{aligned} \tag{16}$$

Coupling between normal and tangential components is achieved through the functions of u_n and u_t.

The cohesive failure model by Geubelle (1995) and Lin et al. (in press) incorporates a bilinear form of the traction–displacement jump relation for mode mixity of applied tractions. The traction-separation law is expressed as

$$\begin{aligned}T_n&=\begin{cases}\dfrac{\sigma_{max}}{\delta_{max}}\delta_n & \text{for } \delta\leqslant\delta_{max},\\ \dfrac{\sigma_{max}}{\delta}\dfrac{1-\delta}{1-\delta_{max}}\delta_n & \text{for } \delta>\delta_{max},\end{cases}\\ T_t&=\begin{cases}\dfrac{\sigma_{max}}{\delta_{max}}\dfrac{u_n^c}{u_t^c}\delta_t & \text{for } \delta\leqslant\delta_{max},\\ \dfrac{\sigma_{max}}{\delta}\dfrac{1-\delta}{1-\delta_{max}}\dfrac{u_n^c}{u_t^c}\delta_t & \text{for } \delta>\delta_{max},\end{cases}\end{aligned} \tag{17}$$

where u_n and u_t are the normal and tangential components of interfacial displacement jump and δ_n, δ_t and δ are the corresponding non-dimensional variables, defined as

$$\delta_t=\frac{u_t}{u_t^c},\quad \delta_n=\frac{u_n}{u_n^c},\quad \delta=\sqrt{\delta_t^2+\delta_n^2}. \tag{18}$$

The parameters u_n^c and u_t^c are critical values of normal and tangential separation, for which complete debonding is assumed to occur. The parameter σ_{max} corresponds to the maximum value of normal traction T_n for a normal displacement jump of $u_n=\delta_{max}u_n^c$. The maximum absolute value of $|T_t|$ is $\tau_{max}=\sigma_{max}(u_n^c/u_t^c)$ which occurs at $|u_t|=(1/2)\delta_{max}u_t^c$. Since the work of separation per unit area on the interface in the normal and tangential directions, are expressed as

$$\Gamma_{\mathrm{n}} = \frac{1}{2}\sigma_{\max} u_{\mathrm{n}}^{\mathrm{c}}, \quad \Gamma_{\mathrm{t}} = \frac{1}{2}\tau_{\max} u_{\mathrm{t}}^{\mathrm{c}}. \tag{19}$$

The maximum tangential traction expression implies that $\Gamma_{\mathrm{n}} = \Gamma_{\mathrm{t}}$, or that the critical energy release rates are the same for mode I and mode II. This constraint, in a sense, creates an equivalence between the potential based models and the non-linear spring relations. Parameters in both classes of models may be adjusted, so that they possess the same essential features, e.g. the fracture energy or the area under the cohesive law, the peak cohesive traction etc. The parameters $u_{\mathrm{n}}^{\mathrm{c}}$, $u_{\mathrm{t}}^{\mathrm{c}}$ or δ^* typically introduce a characteristic length of the material microstructure. A major difference between the two models is that Geubelle's model admits a jump in the slope of the traction–displacement curve, while Needleman's polynomial and exponential models have continuous slopes. Both of these laws are reversible, i.e., they retrace the traction–displacement curve upon unloading. It has been argued (see Camacho and Ortiz, 1996; Ortiz and Pandolfi, 1999) that the decohesion process is expected to exhibit some irreversibility. Following their models, irreversibility is incorporated in the present work by allowing the cohesive surfaces to linearly unload to and reload from the origin.

2.3. Implementation in the Voronoi cell FEM

In implementing the interfacial constitutive relations in VCFEM, relations from the cohesive zone models are substituted in the last two terms in Eq. (2). For Needleman's models this takes the form

$$\begin{aligned} &- \int_{\partial\Omega_{\mathrm{m}}^{\mathrm{c}}/\partial\Omega_{\mathrm{c}}^{\mathrm{c}}} \int_{u_{\mathrm{n}}}^{u_{\mathrm{n}}+\Delta u_{\mathrm{n}}} T_{\mathrm{n}}^{\mathrm{m}}\, \mathrm{d}u_{\mathrm{n}}\, \mathrm{d}\partial\Omega - \int_{\partial\Omega_{\mathrm{m}}^{\mathrm{c}}/\partial\Omega_{\mathrm{c}}^{\mathrm{c}}} \int_{u_{\mathrm{t}}}^{u_{\mathrm{t}}+\Delta u_{\mathrm{t}}} T_{\mathrm{t}}^{\mathrm{m}}\, \mathrm{d}u_{\mathrm{t}}\, \mathrm{d}\partial\Omega \\ &\quad = \int_{\partial\Omega_{\mathrm{m}}^{\mathrm{c}}/\partial\Omega_{\mathrm{c}}^{\mathrm{c}}} [\phi(u_{\mathrm{n}}+\Delta u_{\mathrm{n}}, u_{\mathrm{t}}+\Delta u_{\mathrm{t}}) - \phi(u_{\mathrm{n}}, u_{\mathrm{t}})]\, \mathrm{d}\partial\Omega, \end{aligned} \tag{20}$$

where the potentials $\phi(u_{\mathrm{n}}, u_{\mathrm{t}})$ for polynomial and exponential forms are given in Eqs. (13) and (15). For Geubelle's model the work of separation becomes

$$\begin{aligned} &- \int_{\partial\Omega_{\mathrm{m}}^{\mathrm{c}}/\partial\Omega_{\mathrm{c}}^{\mathrm{c}}} \int_{u_{\mathrm{n}}}^{u_{\mathrm{n}}+\Delta u_{\mathrm{n}}} T_{\mathrm{n}}^{\mathrm{m}}\, \mathrm{d}u_{\mathrm{n}}\, \mathrm{d}\partial\Omega \int_{\partial\Omega_{\mathrm{m}}^{\mathrm{c}}/\partial\Omega_{\mathrm{c}}^{\mathrm{c}}} \int_{u_{\mathrm{t}}}^{u_{\mathrm{t}}+\Delta u_{\mathrm{t}}} T_{\mathrm{t}}^{\mathrm{m}}\, \mathrm{d}u_{\mathrm{t}}\, \mathrm{d}\partial\Omega \\ &\quad = (1-\Psi) \int_{\partial\Omega_{\mathrm{m}}^{\mathrm{c}}/\partial\Omega_{\mathrm{c}}^{\mathrm{c}}} \frac{1}{2}\frac{\sigma_{\max} u_{\mathrm{n}}^{\mathrm{c}}}{\delta_{\max}} \left((\delta_{\mathrm{n}}+\Delta\delta_{\mathrm{t}})^2 + (\delta_{\mathrm{t}}+\Delta\delta_{\mathrm{t}})^2 \right) \mathrm{d}\partial\Omega \\ &\qquad + \Psi \int_{\partial\Omega_{\mathrm{m}}^{\mathrm{c}}/\partial\Omega_{\mathrm{c}}^{\mathrm{c}}} \frac{\sigma_{\max} u_{\mathrm{n}}^{\mathrm{c}}}{1-\delta_{\max}} \left[\sqrt{\delta_{\mathrm{t}}^2 + (\delta_{\mathrm{n}}+\Delta\delta_{\mathrm{n}})^2} + \sqrt{\delta_{\mathrm{n}}^2 + (\delta_{\mathrm{t}}+\Delta\delta_{\mathrm{t}})^2} \right. \\ &\qquad \left. - \frac{1}{2}\left((\delta_{\mathrm{n}}+\Delta\delta_{\mathrm{n}})^2 + (\delta_{\mathrm{t}}+\Delta\delta_{\mathrm{t}})^2 \right) \right] \mathrm{d}\partial\Omega, \end{aligned} \tag{21}$$

where Ψ is a step function defined as

$$\Psi = \begin{cases} 0 & \text{for } \delta \leqslant \delta_{\max}, \\ 1 & \text{for } \delta > \delta_{\max}. \end{cases}$$

In each Voronoi cell element, the matrix-inclusion interface is represented by a set of node-pairs which can facilitate decohesion. The master node in this pair lies in the matrix phase while the slave node belongs to the inclusion phase. The normal and tangential components of displacement jump u_{n} and u_{t} correspond to the separation of these interfacial node-pairs.

2.4. Method of solution

Progressive debonding in composite microstructures is solved using an incremental approach, where a set of element and global equations are solved in each increment for stresses and displacements. The following steps are pursued.

1. Local equations in each element are obtained by substituting stress interpolations (8) and (9) and boundary/interface displacement interpolations (10) in the element energy functional of Eq. (2), and setting variations with respect to the stress coefficients $\Delta\boldsymbol{\beta}^{m}$, $\Delta\boldsymbol{\beta}^{c}$ respectively to zero. This results in the weak forms of the element kinematic relations,

$$\begin{bmatrix} \int_{\Omega_m}[\mathbf{P}^m]^T[\mathbf{S}^m][\mathbf{P}^m]\,d\Omega & [\mathbf{0}] \\ [\mathbf{0}] & \int_{\Omega_c}[\mathbf{P}^c]^T[\mathbf{S}^c][\mathbf{P}^c]\,d\Omega \end{bmatrix} \begin{Bmatrix} \Delta\boldsymbol{\beta}^m \\ \Delta\boldsymbol{\beta}^c \end{Bmatrix} = \begin{bmatrix} \int_{\partial\Omega_e}[\mathbf{P}^m]^T[\mathbf{n}^e][\mathbf{L}^e]\,d\partial\Omega & -\int_{\partial\Omega_c}[\mathbf{P}^m]^T[\mathbf{n}^c][\mathbf{L}^c]\,d\partial\Omega & [\mathbf{0}] \\ [\mathbf{0}] & [\mathbf{0}] & \int_{\partial\Omega_e}[\mathbf{P}^c]^T[\mathbf{n}^c][\mathbf{L}^c]\,d\partial\Omega \end{bmatrix} \begin{Bmatrix} \mathbf{q}+\Delta\mathbf{q} \\ \mathbf{q}^m+\Delta\mathbf{q}^m \\ \mathbf{q}^c+\Delta\mathbf{q}^c \end{Bmatrix} - \begin{Bmatrix} \int_{\Omega_m}[\mathbf{P}^m]^T\{\boldsymbol{\epsilon}^m\}\,d\Omega \\ \int_{\Omega_c}[\mathbf{P}^c]^T\{\boldsymbol{\epsilon}^c\}\,d\Omega \end{Bmatrix} \tag{22}$$

or in a condensed form

$$[\mathbf{H}^e]\{\boldsymbol{\beta}+\Delta\boldsymbol{\beta}\} = [\mathbf{G}^e]\{\mathbf{q}+\Delta\mathbf{q}\} - \{\mathbf{R}_1^e\}. \tag{23}$$

Here $[\mathbf{n}^e]$ and $[\mathbf{n}^c]$ are matrices defined in terms of direction cosines of unit outward normal vectors to the element boundary and matrix-inclusion interface respectively. Eq. (23) is linear and is solved to express the stress coefficients in terms of the nodal displacements.

2. The weak forms of the global traction continuity conditions are subsequently solved by setting the variation of the total energy functional in Eq. (3) with respect to $\Delta\mathbf{q}$, $\Delta\mathbf{q}^m$ and $\Delta\mathbf{q}^c$, to zero. This results in the weak form of the traction reciprocity conditions, stated for both Needleman's and Geubelle's models as:

$$\sum_{e=1}^{N} \begin{bmatrix} \int_{\partial\Omega_e}[\mathbf{L}^e]^T[\mathbf{n}^e]^T[\mathbf{P}^m]\,d\partial\Omega & [\mathbf{0}] \\ -\int_{\partial\Omega_m^c}[\mathbf{L}^c]^T[\mathbf{n}^c]^T[\mathbf{P}^m]\,d\partial\Omega & [\mathbf{0}] \\ [\mathbf{0}] & \int_{\partial\Omega_c^c}[\mathbf{L}^c]^T[\mathbf{n}^c]^T[\mathbf{P}^c]\,d\Omega \end{bmatrix} \begin{Bmatrix} \boldsymbol{\beta}^m+\Delta\boldsymbol{\beta}^m \\ \boldsymbol{\beta}^c+\Delta\boldsymbol{\beta}^c \end{Bmatrix} = \sum_{e=1}^{N} \begin{Bmatrix} \int_{\Gamma_{tm}}[\mathbf{L}^e]^T\{\bar{\mathbf{t}}+\Delta\bar{\mathbf{t}}\}\,d\Omega \\ -\int_{\partial\Omega_m^c}[\mathbf{L}^c]^T(\{\mathbf{n}^c\}T_n(u_n+\Delta u_n, u_t+\Delta u_t)+\{\mathbf{t}^c\}T_t(u_n+\Delta u_n, u_t+\Delta u_t))\,d\partial\Omega \\ -\int_{\partial\Omega_c^c}[\mathbf{L}^c]^T(\{\mathbf{n}^c\}T_n(u_n+\Delta u_n, u_t+\Delta u_t)+\{\mathbf{t}^c\}T_t(u_n+\Delta u_n, u_t+\Delta u_t))\,d\partial\Omega \end{Bmatrix} \tag{24}$$

or in a condensed form

$$\sum_{e=1}^{N}[\mathbf{G}^e]^T\{\boldsymbol{\beta}+\Delta\boldsymbol{\beta}\} = \sum_{e=1}^{N}\{\mathbf{R}_2^e\} \tag{25}$$

Substituting (23) in (25) yields:

$$\sum_{e=1}^{N}[\mathbf{G}^e]^T([\mathbf{H}^e]^{-1}[\mathbf{G}^e]\{\mathbf{q}+\Delta\mathbf{q}\} - \{\mathbf{R}_1^e\}) = \sum_{e=1}^{N}\{\mathbf{R}_2^e\}. \tag{26}$$

The normal and tangential components of the interfacial separation are expressed as

$$\begin{aligned} u_n + \Delta u_n &= \{\mathbf{n}^c\}^T[\mathbf{L}^c]\{\mathbf{q}^m + \Delta\mathbf{q}^m - \mathbf{q}^c - \Delta\mathbf{q}^c\}, \\ u_t + \Delta u_t &= \{\mathbf{t}^c\}^T[\mathbf{L}^c]\{\mathbf{q}^m + \Delta\mathbf{q}^m - \mathbf{q}^c - \Delta\mathbf{q}^c\}. \end{aligned} \tag{27}$$

Eq. (26) is nonlinear due to the relation between interfacial tractions and interfacial displacements in Eqs. (14), (16 and (17). A Newton–Raphson iteration method is consequently invoked to solve for the increments of nodal displacement on the element boundaries and matrix-inclusion interfaces. The linearized form of Eq. (26) for the jth iteration is

$$\sum_{e=1}^{N}[\mathbf{K}^e]^j \begin{Bmatrix} d\mathbf{q} \\ d\mathbf{q}^m \\ d\mathbf{q}^c \end{Bmatrix}^j = \sum_{e=1}^{N}\{\mathbf{R}_2^e\}^j - \sum_{e=1}^{N}[\mathbf{G}^e]^T([\mathbf{H}^e]^{-1}[\mathbf{G}^e]\{\mathbf{q} + \Delta\mathbf{q}\}^j - \{\mathbf{R}_1^e\}). \tag{28}$$

This is iteratively solved to obtain the incremental nodal displacements

$$\{\Delta\mathbf{q}\}^{j+1} = \{\Delta\mathbf{q}\}^j + \{d\mathbf{q}\}^j, \quad \{\Delta\mathbf{q}^m\}^{j+1} = \{\Delta\mathbf{q}^m\}^j + \{d\mathbf{q}^m\}^j, \quad \{\Delta\mathbf{q}^c\}^{j+1} = \{\Delta\mathbf{q}^c\}^j + \{d\mathbf{q}^c\}^j \tag{29}$$

On the matrix-inclusion interface, each node-pair is assumed to be debonded when the factor u_n/δ^* for Needleman's model or δ_n for Geubelle's model exceeds unity.

3. Following the evaluation of nodal displacements, stress coefficients are calculated in each element using the relations (23). The stresses at any location within the element may then be assessed from Eqs. (8) and (9).

3. Numerical examples

The numerical examples are divided into three categories. In the first set of examples, VCFEM results with the interface decohesion model are compared with two established studies in literature for imperfect fiber-matrix interfaces and the evolution of decohesion. The second set of examples is aimed at the evaluation of cohesive parameters by comparison of VCFEM simulations with experimental results and further validation. In the final set, VCFEM simulations are used to make predictions of damage and overall mechanical behavior for fiber reinforced composite microstructures with different morphologies. The stress functions in the inclusion phase of each Voronoi cell element is generated using 33 terms (7th order polynomial stress function, i.e. $p + q = 2..7$) for the polynomial function in Eq. (4). The matrix stress function has an additional 36 reciprocal terms due to the reciprocal terms in Eq. (6) (3 reciprocal terms for each polynomial exponent from 2 to 4, i.e., $i = p + q..p + q + 2\ \forall p + q \in [2, 4]$). Displacement fields on the element boundary and on the matrix and inclusion parts of the interface are represented using linear interpolations $[\mathbf{L}^e]$ and $[\mathbf{L}^c]$ in Eq. (10). The number of node-pairs on the interface is set to 16. This is consistent with the requirements of stability and rank sufficiency of the assumed stress hybrid FEM, as discussed in Moorthy and Ghosh (1996, 2000). The initial locations of interfacial nodes, prior to debonding, are determined by an adaptation procedure that is detailed in Moorthy and Ghosh (2000). In this process, nodes are added or positioned to minimize the error in inter-element and interfacial traction continuity. It results in optimization of the virtual work with respect to traction discontinuity across boundaries. The node-pairs are moved in the direction of the debond once debonding sets in, to accurately capture the crack tip stress concentration.

3.1. Comparison with established results in literature

3.1.1. Problem with imperfect interfaces

In the first example, the behavior under transverse loading of microstructures with debonded fiber-matrix interfaces is simulated by VCFEM and compared with results in Achenbach and Zhu (1990). The representative volume element (RVE) of the microstructure is considered to have a square diagonal arrangement as shown in Fig. 2 with an area fraction of $a_f = 0.4$. The material properties for the elastic matrix are $E_m = 34.684 \times 10^6$ psi, $\nu_m = 0.22$, while those for the elastic fiber are $E_c = 73.2 \times 10^6$ psi, $\nu_c = 0.22$. The interface is modeled in Achenbach and Zhu (1990) and also in the VCFEM analysis with linear springs that have fiber size dependent normal and tangential stiffnesses, expressed as

$$k_r = \frac{k\,G_m}{r}, \quad k_\theta = \frac{k\,G_m}{r},$$

where G_m is the matrix shear modulus, r the fiber radius and k is a constant which is varied from 1 to ∞ to reflect interfacial stiffness. Perfect bonding is manifested by $k \to \infty$. A quarter of the RVE is modeled due to symmetry conditions. For VCFE analysis, the RVE domain is discretized into two Voronoi cell elements, while the boundary element method is implemented in Achenbach and Zhu (1990). Symmetry conditions are applied on two adjacent edges of the computed domain as shown in Fig. 2. The third edge is subjected to a prescribed displacement condition, while the fourth edge is constrained to remain straight and parallel to its original position throughout deformation, implying periodicity.

The distribution of radial stress σ_{rr} along the interface, normalized with the applied far field stress σ_0, are compared in Fig. 3(a) for $k = 1$, 10 and ∞. It asymptotically drops to a minimum value at $\theta = 90°$ from a maximum value at $\theta = 0°$. With increasing interface stiffness or k, the values of σ_{rr} increase rapidly at lower values of k, but the rate slows down at higher values of k. An interface with zero stiffness corresponds to a

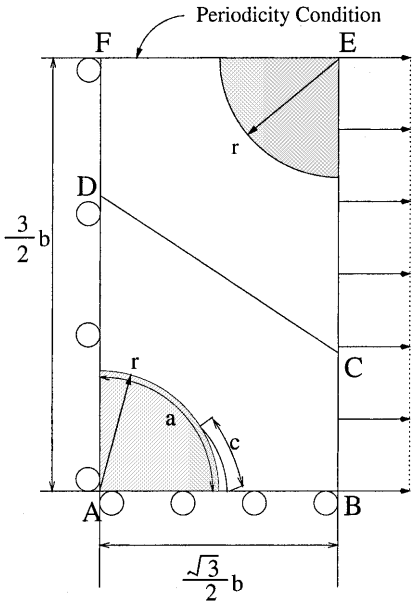

Fig. 2. A VCFE mesh of a composite with hexagonal fiber arrangement subjected to uniform tensile stress as solved in Achenbach and Zhu (1990).

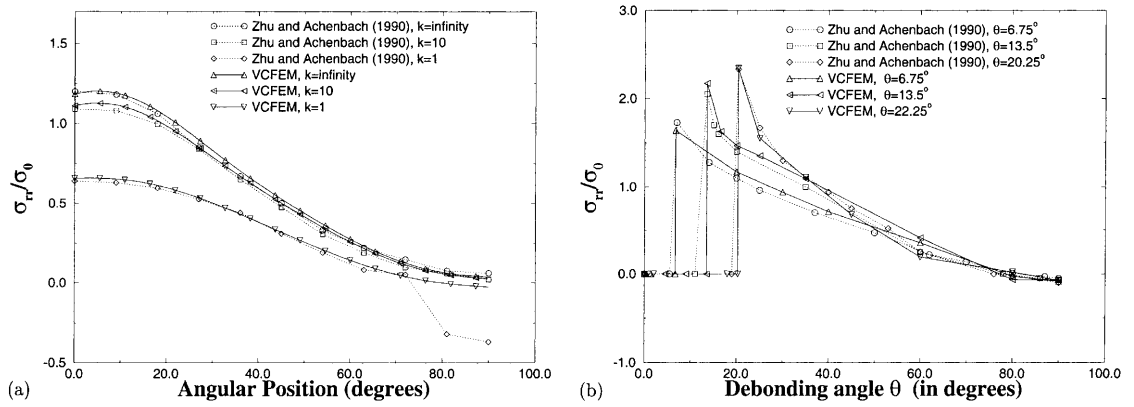

Fig. 3. (a) σ_{rr} stress plots along the perfect interface for various values of stiffness and (b) the radial stress σ_{rr} with various extents of debond.

debonded fiber from matrix and the response is the same as that for a matrix with voids. Excellent agreement of results by VCFEM analysis and those in Achenbach and Zhu (1990), except for when where σ_{rr} becomes compressive (i.e. $\theta > 75°, k = 1$). This is probably due to the implementation of the contact conditions in the compressive region. The compressive contact stresses in VCFEM is modeled using a penalty approach leading to a continuous variation of stresses without the jumps. The radial stresses normalized by the far field stress σ_{rr}/σ_0 are plotted as functions of angular positions for different lengths of the interfacial crack in Fig. 3(b). The stress reaches a peak at the crack tip and the peak increases with increasing debond angle due to increase in average stress. The stress peaks are accurately predicted by VCFEM.

3.1.2. Problem with progressive debonding

In Needleman (1987), the cohesive zone model provides a unified framework for simulating the progress of interfacial decohesion from initiation to arrest, where Eqs. (14) have been used for simulating debonding of an elastic–plastic matrix from rigid spherical reinforcements. The reinforcements of 1.04% volume fraction are arranged in a cylindrical periodic array. Consequently, an axisymmetric analysis of a square unit cell with periodic boundary conditions is conducted. In Needleman's analysis (Needleman, 1987), the matrix is modeled as rate dependent elastic–viscoplastic material with isotropic hardening, with the effective plastic strain rate $\dot{\bar{\epsilon}}$ being expressed in terms of the effective stress $\bar{\sigma}$ as

$$\dot{\bar{\epsilon}} = \dot{\epsilon}_0 \left[\frac{\bar{\sigma}}{g(\bar{\epsilon})} \right]^{1/m}, \quad g(\bar{\epsilon}) = \sigma_0 (1 + \bar{\epsilon}/\epsilon_0)^N, \quad \epsilon_0 = \frac{\sigma_0}{E}, \tag{30}$$

where m and N are the strain rate hardening and strain hardening exponents and σ_0 is a reference strength. The matrix material properties are assumed to be $E_m = 500\sigma_0$, $\nu_m = 0.3$ and $\sigma_0 = 400$ MPa. The current version of VCFEM formulation can only support rate independent plasticity. It is deemed that the small value of the exponent ($m = 0.01$) in Needleman (1987) would agree (at least qualitatively) with the VCFEM results using rate independent plasticity ($m = 0$). The inclusion is modeled as elastic with very high stiffness. The cohesive zone parameters in Eqs. (14) are taken as $\sigma_{max} = 3\sigma_0$, $\delta/r_0 = 0.01$, and $\alpha = 10.0$. The stress triaxiality parameter ρ is set to 0.5. The VCFEM model consists of a single element with periodic boundary conditions imposed as

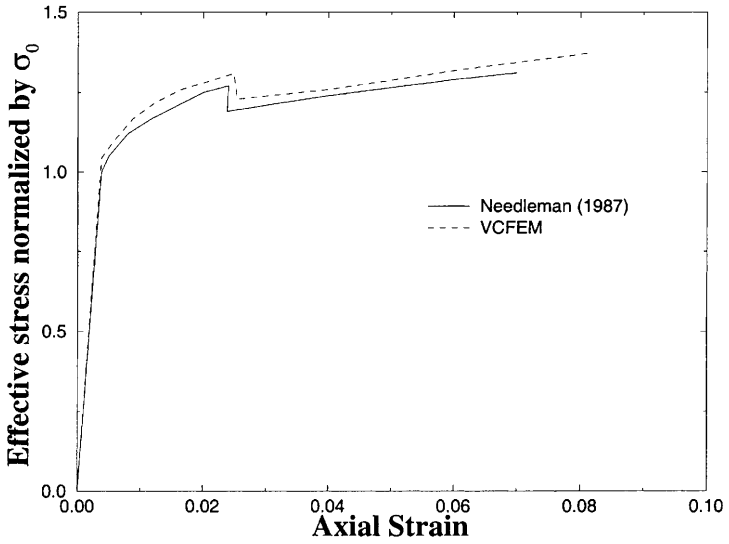

Fig. 4. Plot of the effective stress Σ_e as a function of axial strain ϵ_a for comparison of VCFEM results with those presented in Muskhelishvili (1961).

$$\dot{u}_x = 0, \quad \dot{T}_y = 0 \quad \text{on } x = 0, \tag{31}$$

$$\dot{u}_x = \dot{U}_x = \dot{\epsilon}_\infty b_0, \quad \dot{T}_y = 0 \quad \text{on } x = R_0,$$

$$\dot{u}_y = \dot{U}_y, \quad \dot{T}_x = 0 \quad \text{on } y = R_0. \tag{32}$$

Here, $\dot{u}_x$ and $\dot{u}_y$, and $\dot{T}_x$ and $\dot{T}_y$ are the velocities and traction rates, in the radial and axial directions respectively. The macroscopic effective stress $\Sigma_e = |\Sigma_x - \Sigma_y|$ is plotted as a function of the axial strain $\epsilon_a = \ln(1 + U_x/b_0)$ in Fig. 4. The onset of debonding is signaled by the sudden drop in stress level and its arrest is indicated by the resumption of monotonic increase of flow stress. The results of VCFEM simulation agree rather well with those in Needleman (1987). The slightly higher stress values can be attributed to the small deformation rate independent plasticity with exponent $m = 0$ in VCFEM formulation.

3.2. An experimental-computational study

Prior to predicting the interfacial debonding phenomena for multiple-fiber reinforced composites with the computational model, limited comparisons with experiments are conducted with model composite systems with two objectives. The first is to ascertain the material parameters in the cohesive zone model, viz. σ_{max}, δ^* and α in Needleman's models (Needleman, 1992) and σ_{max}, δ_{max}, u_n^c and u_t^c in Geubelle's model (Lin et al., in press). The parameters are evaluated by solving inverse problems in which the difference between critical experimental observations and results of VCFEM simulations are minimized. The second objective is to validate the predictions of VCFEM against experimental observations for composites with different microscopic architectures.

3.2.1. The experimental procedure

The debonding experiments are conducted with model single and multiple fiber specimens in the form of a cruciform as shown in Fig. 5(a). The cruciform shape has been developed in Gundel et al. (1995), Majumdar et al. (1998), Tandon et al. (1998) to avoid stress singularity at the intersection of fiber-matrix

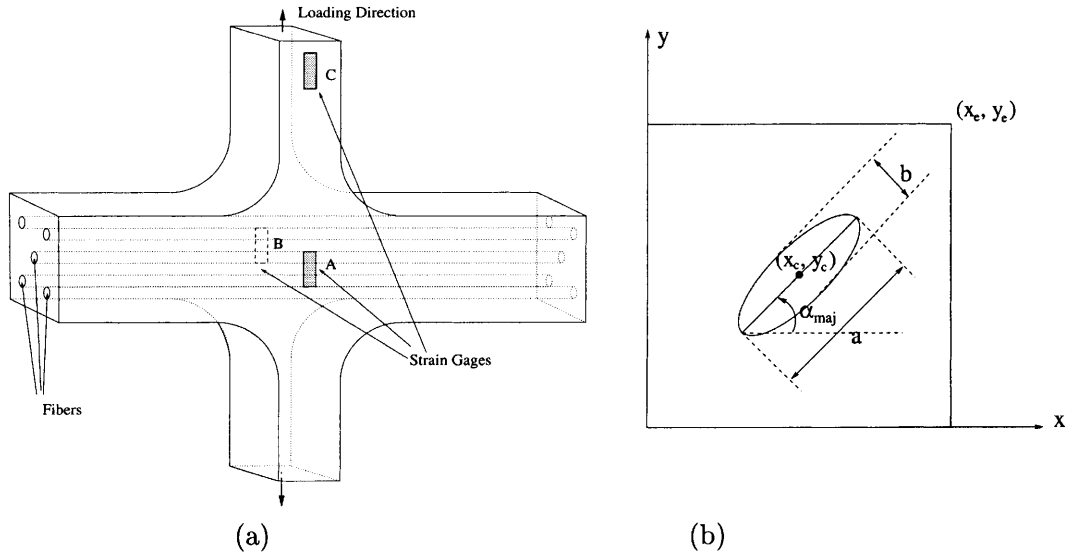

Fig. 5. (a) A schematic diagram of the cruciform specimen with reinforced fibers and applied loading, (b) a typical cross-section delineating geometric parameters of the fiber.

Table 1
Statistics of geometrical parameters in the experimental specimens: (a) specimen number, (b) number of fibers, (c) fiber cross-section, (d) fiber centroidal coordinates (x_c, y_c), (e) dimensions of the cross-section (x_e, y_e), (f) fiber major and minor axes (a, b), (g) cross-sectional area fraction (A_f) and (h) major axis angle with the loading direction (α_{maj})

Specimen #	# Fibers	Shape	x_c, y_c (mm)	x_e, y_e (mm)	a, b (mm)	A_f%	α°_{maj}
1	1	Circular	3.41, 3.0	6.82, 6.0	2.36, 2.36	10.69	–
2	1	Elliptic	3.88, 2.74	7.21, 5.92	3.71, 1.52	10.37	0
3	1	Elliptic	3.78, 3.02	7.21, 5.59	3.71, 1.52	10.99	90
4	5	Circular	2.89, 2.23	7.65, 5.69	0.355, 0.355	1.14	–
4	5	Circular	4.31, 2.23	7.65, 5.69	0.355, 0.355	1.14	–
4	5	Circular	4.22, 3.47	7.65, 5.69	0.355, 0.355	1.14	–
4	5	Circular	2.94, 3.37	7.65, 5.69	0.355, 0.355	1.14	–
4	5	Circular	3.68, 2.78	7.65, 5.69	0.355, 0.355	1.14	–

interface and free surface, that occur in uniform width specimens. Such singularities promote interfacial separation near the free surface and results in invalid interface strength data. The most significant advantage of the cruciform geometry is that it forces debond failure to initiate in the central region of the specimen.

The model composite specimens are fabricated by casting in a cruciform-shaped silicone rubber mold to specimen dimensions, shown in Fig. 5 and Table 1. The circular fillets at the cross junctions reduce stress concentration in the matrix at these locations. The reinforcing fibers in the composite system are stainless steel filaments, which are positioned in the mold and the matrix material is cast around them. Larger diameters, that are helpful in detecting the debond initiation process, are chosen for the single fiber cruciforms. The matrix is an epoxy resin (Epon 828 manufactured by Shell Chemical), that is cured with a polyetheramine (Jeffamine D-230 manufactured by Texaco) for three days at ambient temperature. Room-temperature curing reduces residual thermal stresses in the matrix, due to mismatch in the fiber and matrix

thermal properties, to a minimum. The epoxy matrix is transparent and allows visualization of the debonding process at the fiber-matrix interface. Preliminary experiments with no interfacial coating indicate that the bond strength is high and interface failure progresses rapidly to cause immediate catastrophic rupture. Consequently, the steel filaments are cleaned and polished with acetone and coated with a very thin film of freekote (<0.1 μm) prior to casting the specimens. The freekote imparts a weak strength to the steel–epoxy interface. This allows a somewhat stable growth of the debond crack to permit determination of cohesive zone parameters.

In the experimental set up, three strain gages (**A**, **B** and **C**) are affixed on faces of the specimen as shown in Fig. 5(a). Two gages (**A** and **B**) are located in the central portion of the cruciform in vicinity of potential debond sites. Thus their readings are assumed to correspond to the debonding strains. The third gage **C** is mounted on the limb, away from the fibers and represents the far-field strain. Furthermore, to prevent specimen failure in the grip region, fiber–glass/epoxy end tabs are adhesive bonded on the upright portion of the specimen. Four different microstructural architectures are considered for the experiments. They are:

- Specimen # 1 containing a single circular fiber.
- Specimen # 2 containing a single elliptical fiber with major axis along the loading direction ($\alpha_{maj} = 0°$).
- Specimen # 3 containing a single elliptical fiber with major axis perpendicular to the loading direction ($\alpha_{maj} = 90°$).
- Specimen # 4 containing five identical circular fibers.

These are schematically illustrated in Fig. 5 and the geometric details on location, size etc. are given in Table 1. The area fraction in the table are for the cross-section at the outer edge. The elastic material properties for the reinforcing steel fibers and epoxy matrix are experimentally determined as:

- Young's modulus $E_{steel} = 210$ GPa;
- Poisson's ratio $\nu_{steel} = 0.3$;
- Young's modulus $E_{epoxy} = 4.6$ GPa;
- Poisson's ratio $\nu_{epoxy} = 0.4$.

The cohesive properties of the debonding material are evaluated by solving an inverse problem discussed in Section 3.2.3.

The model specimens are loaded in tension on a servo-hydraulic testing machine. The onset of fiber-matrix debonding is identified with a sharp change in the slope of the stress–strain curve based on strain gage readings at the cruciform center. Acoustic emission sensors are also employed to confirm the onset of debonding. In Fig. 7, the abrupt change in slope at B corresponds to debond initiation, and the relatively flat portion BC corresponds to the strain jump. Subsequent loading along CD proceed with a lower stress–strain slope, due to a reduced load carrying capability of the partially debonded fiber. Unloading along DA and subsequent reloading along ACD indicate no further change in slope, i.e. no additional debonding. Matrix cracks always initiate at the fiber-matrix debond site and grow rapidly to cause specimen failure. Loading is halted prior to fracture in a few specimens, to allow observation of the partially debonded interface.

Following interface failure, the cruciform specimens are sectioned at the center along the loading direction. A drop of a fluorescent dye penetrant is positioned above the sectioned fiber and vacuum infiltration is used to force the penetrant into the debonded interface. The sectioned face is then polished to remove traces of the dye from the original drop. The fiber is then viewed under an ultraviolet light, which cause the regions containing the dye to remain bright in an otherwise dark background. Fig. 6(a) shows the debond under oblique incidence, where the fiber surface is visible through the transparent matrix. The bright regions correspond to locations of debond that are concentrated on the loading axis. Fig. 6(b) shows the cross section of the fiber at a higher magnification, and the debonded region is the thin bright strip along the fiber periphery. The ends of the debond are highlighted by the arrows, and the loading direction is horizontal in the figure. The total angle of debond is estimated from Fig. 6(b) as approximately 85°.

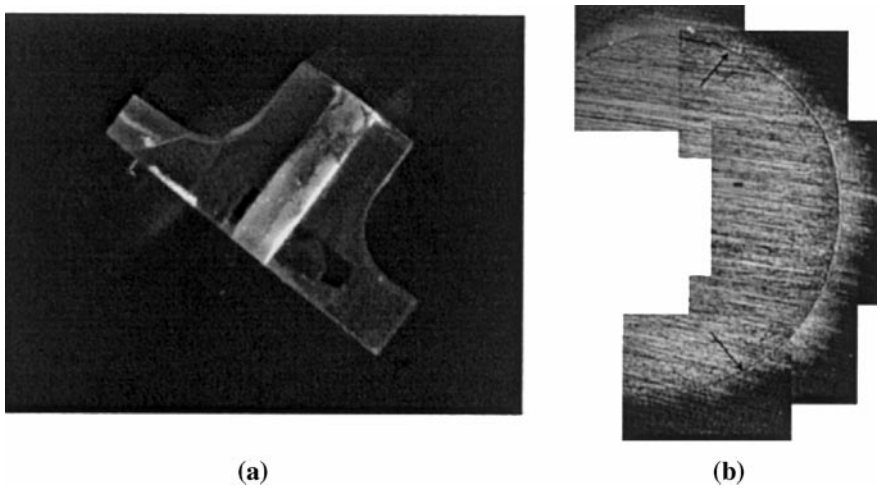

Fig. 6. (a) Faceview of the debonded cruciform specimen showing dye penetration. (b) The cross section indicating debonding angle as the limits of the dye penetrated region.

3.2.2. Evaluation of a conversion factor for 3D to 2D analysis

The experimental results are compared with results of simulations by a 2D (plane strain) Voronoi cell finite element model for parameter identification, validation and damage prediction. While the fiber reinforced cruciform specimen represents a 3D problem in actuality, the stresses and displacements at the center of the cruciform can be well approximated by 2D solutions for a reasonably slender geometry. A conversion factor is therefore established for predicting the 3D stress state from 2D simulations. A full 3D analysis of the cruciform specimen (shown in Fig. 5) and a plane strain analysis of the section containing a single circular fiber of diameter 2.36 mm are conducted using the commercial finite element package

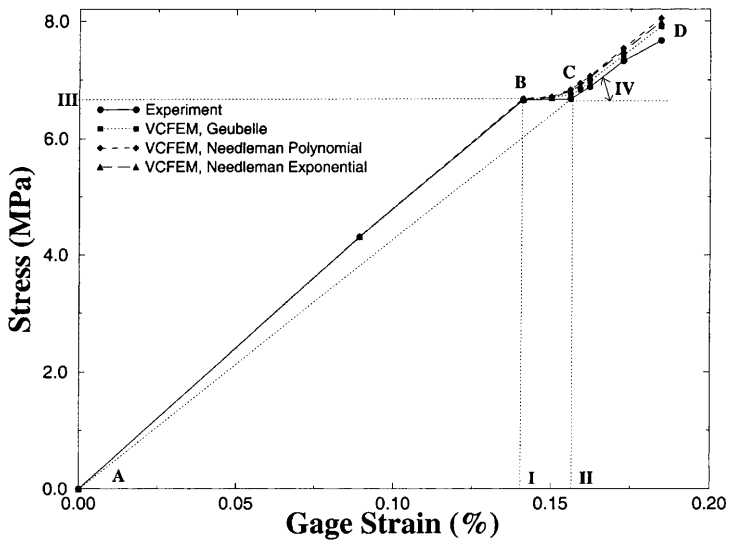

Fig. 7. Macroscopic pre- and post-debonded stress–strain response of the specimen with a single reinforced circular fiber. The roman numerals (I, II, III and IV) correspond to critical property values that are used to calibrate the cohesive zone model.

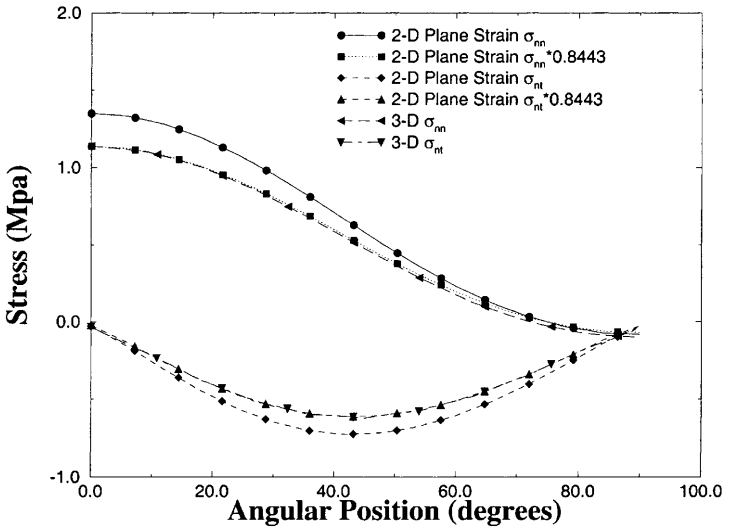

Fig. 8. A plot of the normal and tangential stresses at a perfect interface by ANSYS, for obtaining the conversion factor between 3D and 2D analysis.

ANSYS. The vertical stem (perpendicular to the fiber direction in Fig. 5) of the cruciform has a height of 30 mm (z-axis) and a cross-section of 6 mm (x-axis) $\times$ 6 mm (y-axis). A perfect interface with no debonding is assumed in these analyses. In 2D, a 15 mm $\times$ 6 mm quarter of a vertical section of the cruciform is analyzed. A quarter of the fiber cross-section is located at the corner of this section. A constant stress load is applied on the top surface of the vertical stem as shown in Fig. 5. For the 2D model, this corresponds to a constant stress load on the edge, away from the fiber. Symmetric displacement conditions are applied to two other adjacent edges of the rectangle, while the fourth edge is traction free.

A comparison of the radial stress σ_{rr} and tangential stress $\sigma_{r\theta}$ along the interface by the 2D and 3D analyses is presented in Fig. 8. A stress concentration factor (SCF) is defined as a ratio of the maximum radial stress along the tensile axis (at the pole corresponding to angle $= 0°$ in Fig. 8) of the fiber-matrix interface, to the far-field applied stress. This factor is computed to be $SCF_{2D} = 1.349$ for 2D and $SCF_{3D} = 1.139$ for 3D analyses. By multiplying the plane strain results with a factor $k = SCF_{2D}/SCF_{3D} = 0.844$, a very good match with the 3D solution is obtained. This is shown in the stress plots of Fig. 8. Consequently, the 2D stresses from VCFEM analysis are multiplied by the factor $k = 0.844$ for comparison with 3D experimental results.

3.2.3. Evaluation of cohesive zone parameters

Cohesive zone parameters for the models proposed by Needleman (1987, 1990), Geubelle (1995) and Lin et al. (in press) are calibrated by solving an inverse problem using the VCFE model and comparing with experimental results. The computational model consists of 2D sections with dimensions 33 mm $\times$ y_e, where y_e corresponds to the cross-section height as shown in Fig. 5(b). Values of x_e, y_e, representing the central cross-section of the cruciform, are presented in Table 1. The section is analyzed under plane strain conditions with loading along the x-axis. A total of $(n + 2)$ Voronoi cell elements are used for analyzing a section with n fibers. The n Voronoi cell elements are for the n fibers in the central cross-section portion (Fig. 5(b)) while two additional elements are for the stem portion. In Geubelle's model, the parameters to be determined are δ_{max}, σ_{max}, u_t^c and u_n^c, while in Needleman's model the parameters are σ_{max}, δ^* and α. Their evaluation for a given bonding material (freekote in this problem) follows a multi-variable optimization

process, in which, four *key* variables are chosen for minimizing the difference between experimental and computational results. These effective values are marked as I, II, III, IV in Fig. 7 and are: (i) the strain at which debonding initiates (S_{I}), (ii) the strain (S_{II}) at which debonding arrests, (iii) the stress (S_{III}) at which debonding arrests, and (iv) post debonding slope of the stress–strain plot (S_{IV}). The major steps in this evaluation process are:

1. For each of the models in Eqs. (14), (16) and (17), the overall stress–strain response with debonding behavior is first determined (similar to Fig. 7) for different cohesive parameters. These are chosen arbitrarily from a range of expected parameter values. For each set of parameters, e.g. ($\delta_{\max}$, $\sigma_{\max}$, $u_{\mathrm{t}}^{\mathrm{c}}$, $u_{\mathrm{n}}^{\mathrm{c}}$) or ($\sigma_{\max}$, δ^* and δ^*), an independent VCFEM simulation of debonding in the microstructure is performed.
2. The key variables S_i $(i = \mathrm{I}, \ldots, \mathrm{IV})$ are represented as polynomial functions of the cohesive zone parameters. This produces continuous functions for gradient based optimization methods that are necessary for parameter evaluation. For Geubelle's model (Lin et al., in press; Geubelle, 1995), these are written as

$$S_i = \left(a_{i0} + a_{i1}\delta_{\max} + a_{i2}\delta_{\max}^2 + \cdots\right) + \left(b_{i0} + b_{i1}\sigma_{\max} + b_{i2}\sigma_{\max}^2 + \cdots\right) + \left(c_{i0} + c_{i1}u_{\mathrm{t}}^{\mathrm{c}} + c_{i2}u_{\mathrm{t}}^{\mathrm{c}^2} + \cdots\right) + \left(d_{i0} + d_{i1}u_{\mathrm{n}}^{\mathrm{c}} + d_{i2}u_{\mathrm{n}}^{\mathrm{c}^2} + \cdots\right) \tag{33}$$

while for Needleman's model (Needleman, 1987, 1990), these are

$$S_i = \left(a_{i0} + a_{i1}\sigma_{\max} + a_{i2}\sigma_{\max}^2 + \cdots\right) + \left(b_{i0} + b_{i1}\delta^* + b_{i2}\delta^{*^2} + \cdots\right) + \left(c_{i0} + c_{i1}\alpha + c_{i2}\alpha^2 + \cdots\right). \tag{34}$$

3. Approximately 150 VCFEM simulations are conducted with different parameter sets, to evaluate the coefficients of the polynomial expansions i.e. $a_{i0}, a_{i1}, \ldots,\ b_{i0}, b_{i1}, \ldots,\ c_{i0}, c_{i1}, \ldots, d_{i0}, d_{i1}, \ldots$ For each simulation the computed values of $S_i,\ i = \mathrm{I}, \ldots, \mathrm{IV}$, are recorded from the stress–strain plots. The minimum number of simulations correspond to the total number of unknown coefficients. However, a higher number is performed in this study to accommodate a broad range of cohesive parameters.
4. The coefficients $a_{i0}, a_{i1}, \ldots, b_{i0}, b_{i1}, \ldots, c_{i0}, c_{i1}, \ldots, d_{i0}, d_{i1}, \ldots$ are evaluated by a least square based minimization process using MATLAB. The functions $S_i,\ i = \mathrm{I}, \ldots, \mathrm{IV}$, can then be constructed.
5. Parameters of the cohesive zone models are finally obtained by minimizing the difference between experimental and simulated values of the key variables S_i in the stress–strain plots of Fig. 7 or 12. A multiparameter optimization problem is solved as

$$\begin{aligned} &\text{Minimize}\left[\sum_{i=1}^{4} w_i\left(S_i^{\text{simulation}} - S_i^{\text{experiment}}\right)^2\right] \\ &\text{w.r.t. } \sigma_{\max},\ \delta_{\max},\ u_{\mathrm{n}}^{\mathrm{c}} \quad \text{and} \quad u_{\mathrm{t}}^{\mathrm{c}} \\ &\text{or} \\ &\text{w.r.t. } \sigma_{\max},\ \delta^* \quad \text{and} \quad \alpha. \end{aligned} \tag{35}$$

The weights w_i may be suitably chosen to impart preferential importance to the key variables. Equal weights are chosen for this analysis.

Two sets of resulting values of the cohesive zone parameters are given in Table 2. The first set corresponds to values that are evaluated by comparison with results of specimen 1 experiments. When these parameters are used to simulate the other specimens 2, 3 and 4, it is seen that the maximum difference between experiments and simulations occur for specimen 3. A second set of parameters are consequently derived using the key variables S_i for both specimens 1 and 3, shown in Figs. 7 and 12. A small difference is noted in Table 2, between the values of the two sets. The results shown in the following sections are with the second set of cohesive parameters.

Table 2
The cohesive zone parameters for the three models, viz. Geubelle, Needleman (polynomial) and Needleman (exponential) evaluated from the specimen 1 only and specimens 1 and 3 combined

Model	Specimen #	δ_{max}	σ_{max} (GPa)	u_t^c (mm)	u_n^c (mm)
Geubelle	1 only	0.9412	0.012846	0.00007392	0.00006407
Geubelle	1 & 3	0.9347	0.012570	0.00007217	0.00006395
	Specimen #	σ_{max} (GPa)	δ^* (mm)	α	
Needleman (polynomial)	1 only	0.014613	0.00004837	0.7104	
Needleman (polynomial)	1 & 3	0.014428	0.00004889	0.7116	
Needleman (exponential)	1 only	0.014980	0.00005019	0.6841	
Needleman (exponential)	1 & 3	0.014831	0.00005007	0.6887	

3.2.4. Comparison of VCFEM and experimental results

VCFEM simulations for the plane section of the cruciform, under tensile loading, are conducted for the four different microstructures of specimens 1, 2, 3 and 4. The results are compared with experiments, macroscopically in Figs. 7, 12 and 17 and microscopically in Fig. 6. The abscissa in Figs. 7, 12 and 17 is the gage strain recorded by 0.8 mm strain gages mounted on the specimen surface (A in Fig. 5(a)). The corresponding strains in VCFEM analyses are calculated from the change in length of a 0.8 mm segment, located on the 2D specimen boundary, closest to the fiber. In Table 3, the simulated gage strains and the

Table 3
Results of VCFEM simulation with Geubelle's model: (i) the undamaged stiffness or slope of the undamaged stress–strain plot E_{ud}, (ii) the damaged stiffness or slope of the damaged stress–strain plot E_d, (iii) the change in stiffness, (iv) the averaged tensile strain at the onset of debonding ϵ_{in}^a, (v) the corresponding gage strain ϵ_{in}^g and (vi) the final debonded angle θ_d°

Specimen #	K_{ud} (MPa)	K_d (MPa)	ΔE (%)	Averaged ϵ_{in}^a (%)	Gage ϵ_{in}^g (%)	θ_d°
1	4974	4265	14.25	0.140	0.141	91
2	5249	4621	11.96	0.066	0.063	46
3	5163	3581	30.64	0.145	0.111	134
4	4821	4682	2.88	0.139	0.138	87 (all)

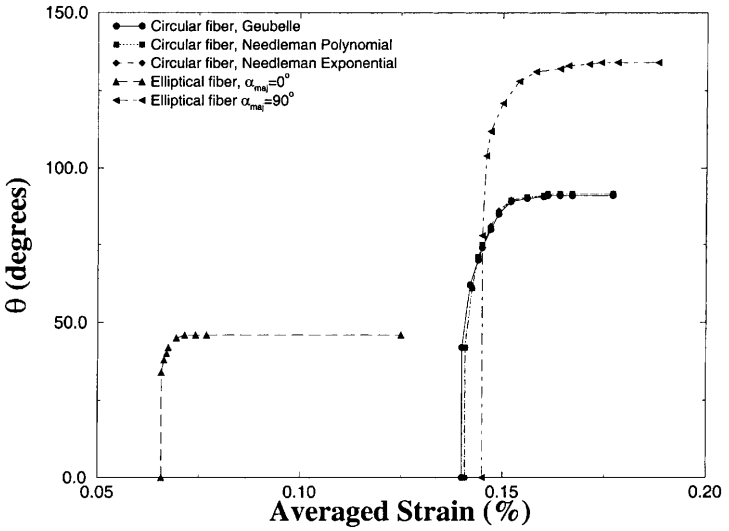

Fig. 9. Plot of the debonding angle θ as a function of average strain, with different cohesive zone models.

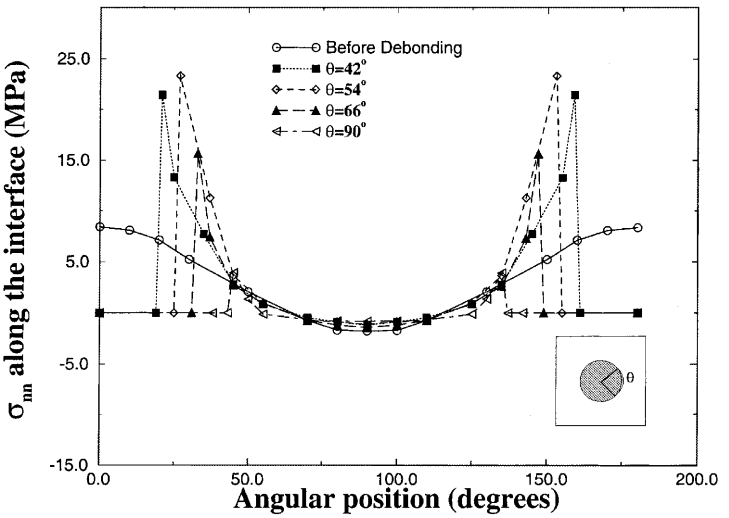

Fig. 10. Distribution of the normal stress σ_{nn} along the interface for increasing values of the debonded angle θ with the circular fiber.

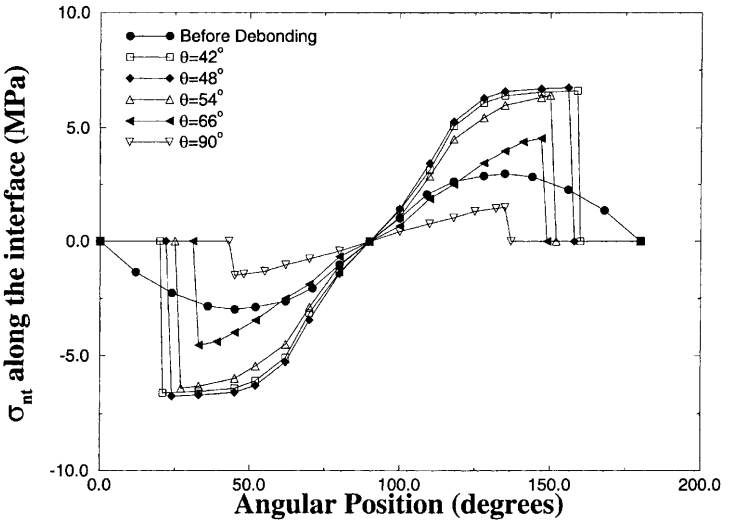

Fig. 11. Distribution of the tangential stress σ_{nt} along the interface for increasing values of the debonded angle θ with the circular fiber.

area-averaged strains are tabulated. There is a small difference between the two strains. This may be attributed to the fact that the edge along which the gage strain is measured is very close to the fibers, which local fluctuations due to the interface prevail. The ordinate in the plots of Figs. 7, 12 and 17 are the area-averaged macroscopic stresses in the direction of loading. The stress–strain plots for all three decohesion models in Fig. 7 show good agreement with the experimental stress–strain behavior. The onset of debond, signaled by a sharp reduction of slope, is also predicted quite well. However, the arrest of debond, as indicated by the change in the post-decohesion stiffness, is more gradual for the simulations than for experiments.

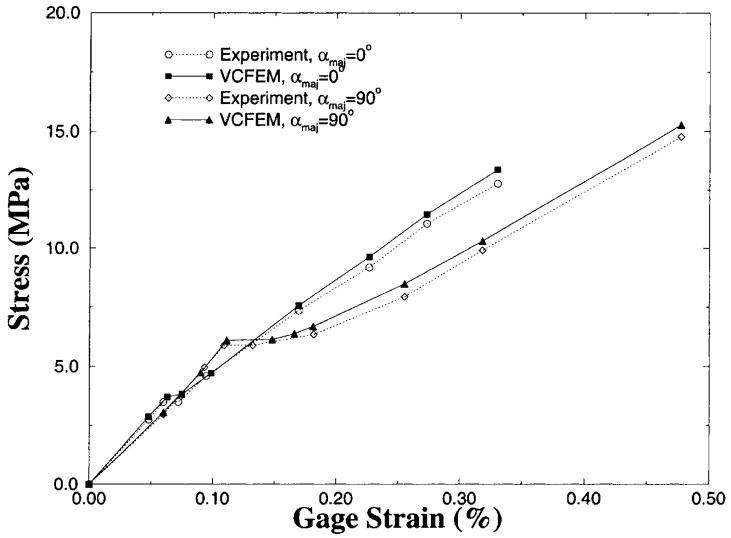

Fig. 12. Macroscopic pre- and post-debonded stress–strain response of the specimen with a single reinforced elliptical fiber oriented along and perpendicular to the loading axis.

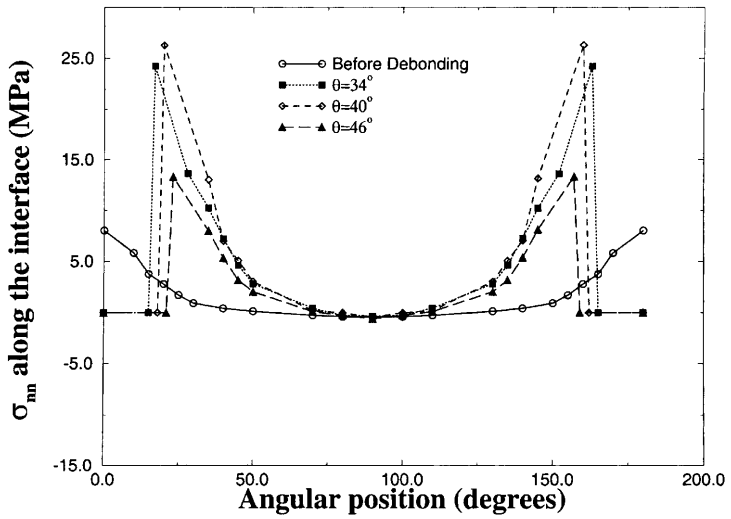

Fig. 13. Distribution of the normal stress σ_{nn} along the interface for increasing values of the debonded angle θ with the elliptical fiber ($\alpha_{maj} = 0°$).

The experimental debonding angle (Fig. 6) is evaluated to be approximately 85°. The corresponding simulated value is found to be 91° (see Table 3). This corresponds to a 6.6% difference from experiments. Table 3 also presents the overall stiffness values before and after debonding and the total debonding angle along the interface, using Geubelle's model (Lin et al., in press). The undamaged overall stiffness K_{ud} is the slope of the area averaged tensile stress–strain plots in the loading direction, for the rectangular section through the cruciform center. The highest K_{ud} is observed for specimen 2 with $\alpha_{maj} = 0°$, while the lowest is that for specimen 4 with a lower volume fraction. The maximum drop in stiffness occurs with specimen 3

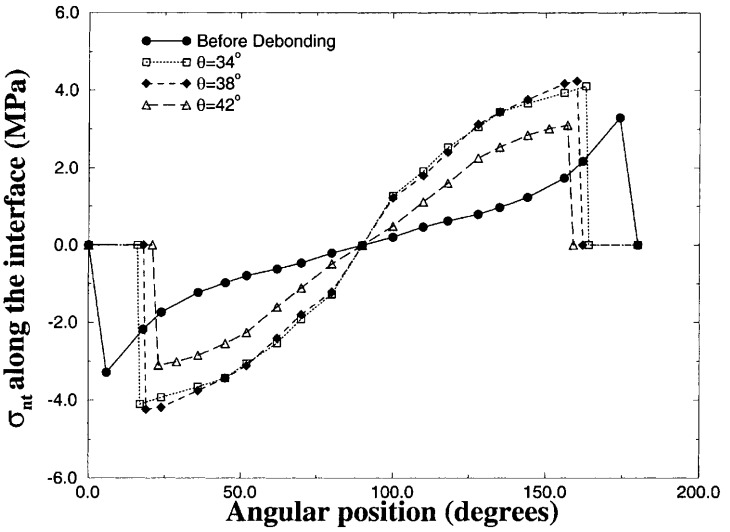

Fig. 14. Distribution of the tangential stress σ_{nt} along the interface for increasing values of the debonded angle θ with the elliptical fiber ($\alpha_{maj} = 0°$).

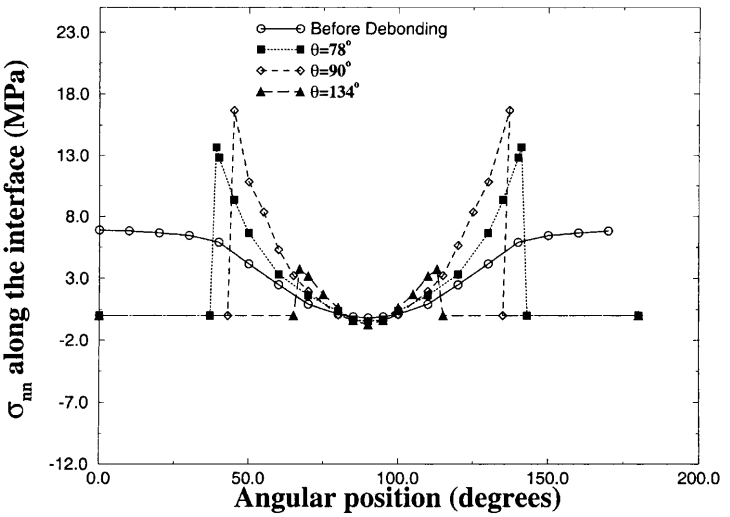

Fig. 15. Distribution of the normal stress σ_{nn} along the interface for increasing values of the debonded angle θ with the elliptical fiber ($\alpha_{maj} = 90°$).

($\alpha_{maj} = 90°$) since this interface undergoes the largest debonding angle ($\theta_d = 134°$). The minimum drop is for the multiple fiber specimen even with considerable interfacial debonding ($\theta_d = 87°$), mainly due to the small area fraction. The increase in debonding angle, as function of the averaged strain, is plotted in Figs. 9 and 18. For specimen 1, the response of the three interfacial decohesion models are extremely close. The debonding angle increases rapidly after initiation with little additional strain, and then tapers off asymptotically to a stable value. The initiation strains for specimens 1 and 3 are quite close, while that for the

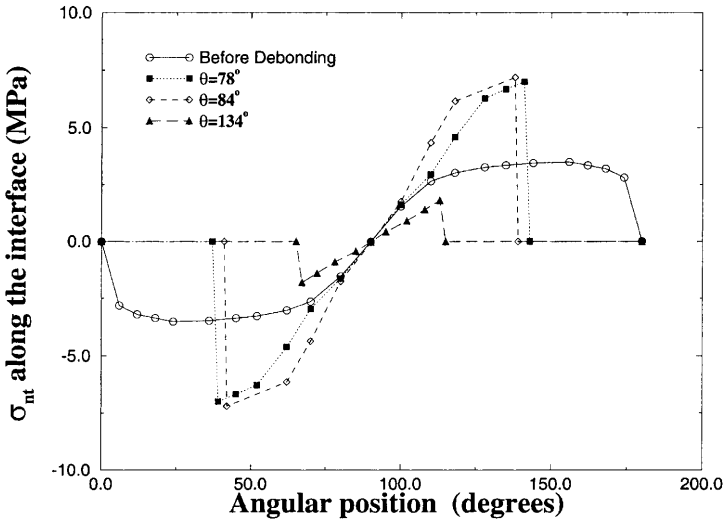

Fig. 16. Distribution of the tangential stress σ_{nt} along the interface for increasing values of the debonded angle θ with the elliptical fiber ($\alpha_{maj} = 90°$).

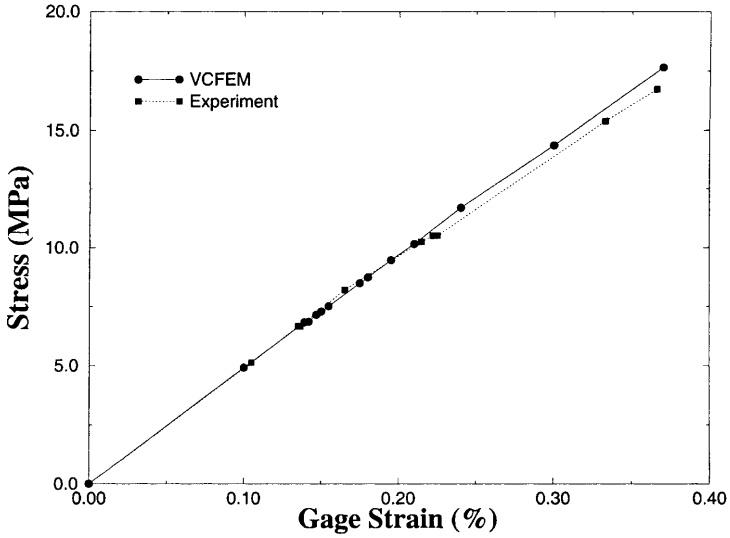

Fig. 17. Macroscopic pre- and post-debonded stress–strain response of the specimen with five circular fibers.

specimen 2 is significantly lower. Also the smallest stable debond angle occurs with the specimen 2 and the largest for specimen 3 with specimen 1 in the middle. The stable debonding angle for both specimens 1 and 4 with circular fibers are quite close.

To understand the effects of stress distribution on the debonding process, the normal and tangential interfacial stresses σ_{nn} and σ_{nt} are plotted from $\phi = 0°$ (the loading direction) to $\phi = 180°$, in Figs. 10, 11, 13–16. The peak stress at the tip of the crack or debond is obtained from the spring tractions at the node-pair, just ahead of the debonded nodes where the condition $\delta = 1$ in Eq. (18) is satisfied. The normal stress

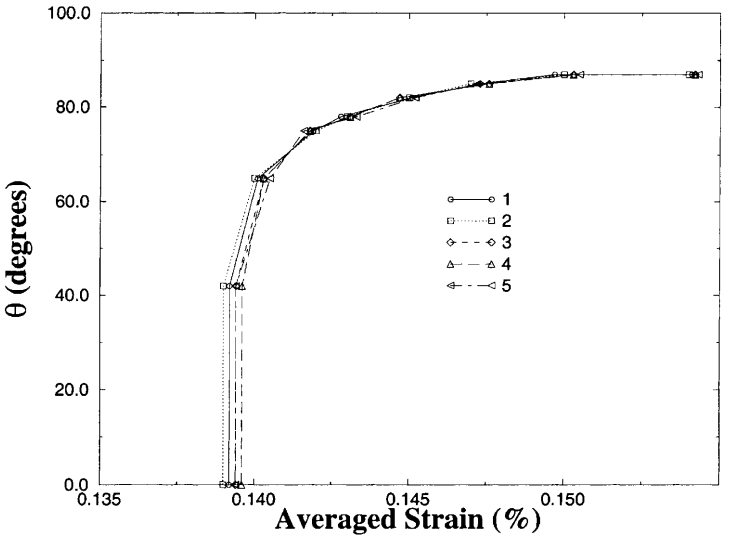

Fig. 18. Plot of the debonding angle θ as a function of strain, for each fiber in the multi-fiber specimen.

plots are symmetric about the angular position $\phi = 90°$, while the tangential stresses are antisymmetric about this angle. Prior to debonding, the normal stress is maximum at $\phi = 0°$, while the shear stress peaks out at $\phi = 45°$. Once debonding initiates, the peaks occurs at the crack tip and subsides monotonically till it reaches the pole at $\phi = 90°$, where σ_{nn} is mildly compressive. With progressive debonding, the peak tensile stress σ_{nn} initially increases in magnitude but subsequently decreases. This behavior may be explained as a consequence of two competing phenomena, viz. an increase in average stress due to increasing debond length and a decrease in the normal component of stress with increasing angular orientation, especially as $\phi \to 90°$. The compressive region also increases with increasing decohesion. Similar observations have also made in Achenbach and Zhu (1990). For the tangential stress σ_{nt}, the maximum value at the crack tip is also found to first increase slightly and then decrease with progressive debonding. From these plots, it is easy to explain the reasons for the nucleation and progress in decohesion, as depicted in Figs. 9 and 18.

Through a combination of experimental and computational simulations, these examples establish considerable confidence in the model for understanding the behavior of the interfacial debonding phenomena.

3.3. Multiple fibers in the microstructure

In this final set of examples, computational analyses are conducted to understand the effect of morphology and applied boundary conditions on the initiation and progress of debonding induced damage in microstructures containing multiple fibers. The microstructure in these examples contain 100 identical circular fibers in a square region corresponding to 20% area fraction.

1. A uniformly dispersed square array (Fig. 19(a)).
2. A randomly dispersed microstructure (Fig. 19(b)).

For comprehending the role of boundary conditions on the damage evolution process, two in-plane conditions, viz. (a) periodic conditions and (b) displacement (non-periodic) boundary conditions, are specified. The periodicity boundary conditions require edges to remain straight and parallel to the original direction throughout deformation by imposing the following conditions:

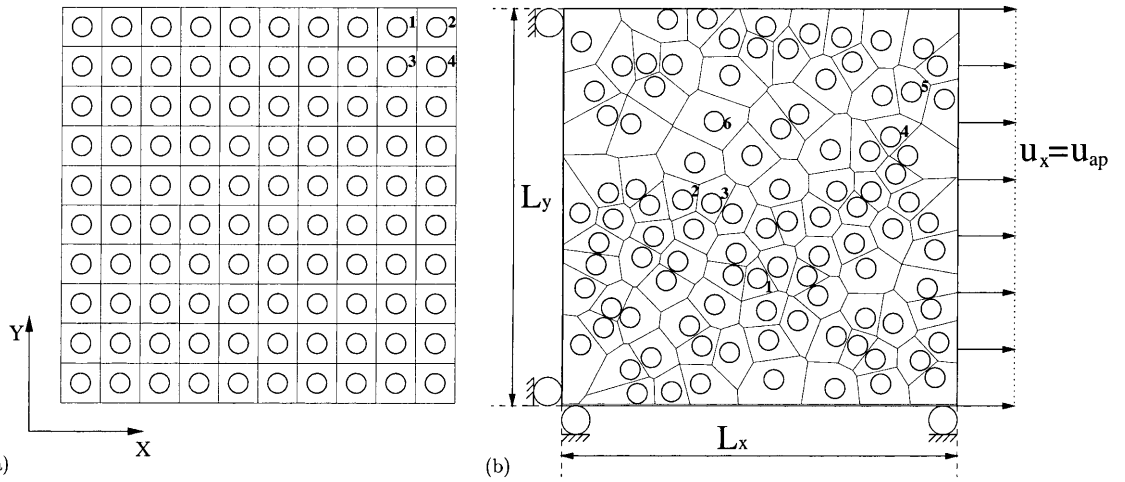

Fig. 19. Tessellated mesh of Voronoi elements for microstructures containing 100 fibers with area fraction = 20%: (a) uniform distribution; (b) random distribution.

$$u_x = 0 \quad (\text{on } x = 0), \quad u_y = 0 \quad (\text{on } y = 0), \quad u_x = u_{\text{ap}} \quad (\text{on } x = L_x), \quad u_y = D_y^{\star} \quad (\text{on } y = L_y),$$
$$T_y = 0 \quad (\text{on } x = 0 \text{ and } x = L_x), \quad T_x = 0 \quad (\text{on } y = 0 \text{ and } y = L_y), \tag{36}$$

where u_{ap} is a monotonically increasing applied displacement and $D_y^{\star}$ is determined from the average force condition $\int_X T_x \, dx = 0$ on $y = L_y$. For the displacement boundary conditions,

$$u_x = T_y = 0 \quad (\text{on } x = 0), \quad u_y = T_x = 0 \quad (\text{on } y = 0), \quad u_x = u_{\text{ap}} \quad (\text{on } x = L_x),$$
$$T_x = T_y = 0 \quad (\text{on } y = L_y). \tag{37}$$

The elastic material properties for the reinforcing steel fibers and epoxy matrix are:

- Young's modulus $E_{\text{steel}} = 210$ GPa;
- Poisson's ratio $\nu_{\text{steel}} = 0.3$;
- Young's modulus $E_{\text{epoxy}} = 4.6$ GPa;
- Poisson's ratio $\nu_{\text{epoxy}} = 0.4$.

The interface is represented by the cohesive zone model of Lin et al. (in press) with the parameters: $\delta_{\max} = 0.9347$, $\sigma_{\max} = 0.012570$ GPa, $u_{\text{t}}^{\text{c}} = 0.00007217$ mm and $u_{\text{n}}^{\text{c}} = 0.00006395$ mm. The plane strain Voronoi cell finite element model is used in this analysis, with a tessellated mesh of 100 Voronoi elements each containing a fiber. For the uniform distribution, the tessellation process yields square elements, while for the random distribution the cells have variable number of edges as shown in Fig. 19(a) and (b).

The macroscopic or area-averaged stress–strain response for the two architectures are plotted for the two boundary conditions in Fig. 20(a). Prior to debonding, the stiffness of the random microstructure is marginally higher than that for the uniform one. For each microstructure, the behavior is stiffer with periodicity. This is due to the additional displacement constraint imposed by periodicity which raises stresses in the microstructure. Appreciable debonding in fibers is signaled by an abrupt change in slope of the stress–strain curve. This is noticed at a significantly smaller strain for the random microstructure. However, the ultimate loss of stiffness is higher for the uniform microstructure. The number of debonded fibers as a function of increasing strain is plotted in Fig. 20(b). The rate of damage growth is more gradual for the random microstructure. This rate is initially low, but increases considerably with straining in the intermediate region and finally tapers off at higher values of strain. This is because initial stages of debonding

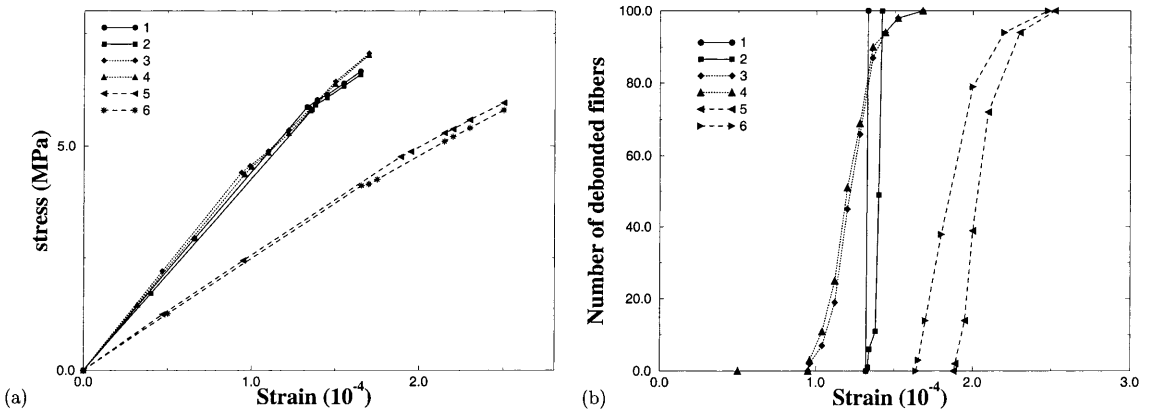

Fig. 20. (a) Macroscopic pre- and post-debonded stress–strain response of the microstructures containing 100 circular fibers and (b) the microscopic plot of the number of debonded fibers as a function of strain. The size cases in parathesis are: (1) vf = 20%, UD–US–PE, (2) vf = 20%, UD–US–DI, (3) vf = 20%, RD–US–DI, (4) vf = 20%, RD–US–PE, (5) vf = 10%, RD–US–DI and (6) vf = 10%, RD–RS–DI, where UD/RD = uniform/random dispersion, US/RS = uniform/random size and PE/DI = periodicity/displacement boundary condition.

are influenced by the inter-fiber spacing. Interfaces of fibers that are in close proximity are damaged early. The subsequent stages of damage also depend on the overall strain state. In the uniform model, the initiation takes place later but the growth of damage by interfacial decohesion occurs rapidly. This is particularly true for the periodic boundary condition. With the displacement boundary conditions, the growth is slow in the beginning but increases substantially with straining.

A clear delineation of the debonding process is obtained from the contour plots of the tensile stress σ_{xx} in Figs. 21 and 22, which show debonds as well as locations of stress concentrations. For the uniform microstructure with displacement boundary conditions (non-periodic), debonding starts at the fiber in the upper right corner and propagates down along the diagonal to create a dominant damage path. The reason for the damage propagation along a distinct path is explained from the radial stress σ_{rr} plots along the interfaces, in Fig. 23. The fiber numbers 1, 2, 3, and 4 are delineated in Fig. 19(a). At a macroscopic strain value of $\epsilon = 1.31 \times 10^{-4}$, just before initiation, the radial stress at the interface of the corner fiber 2 is higher

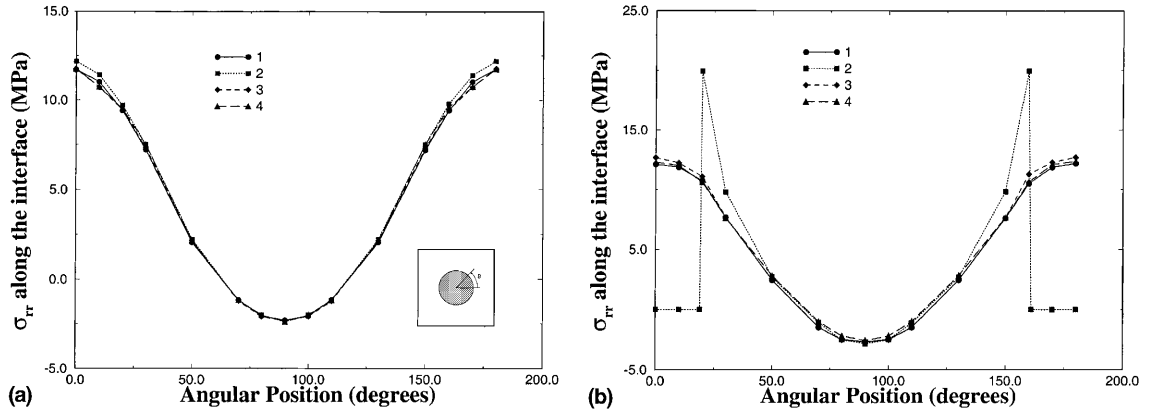

Fig. 21. Distribution of the radial stress σ_{rr} along the interface for different fibers (1, 2, 3 and 4) in the microstructure with displacement boundary conditions for (a) $\epsilon = 1.31 \times 10^{-4}$ and (b) $\epsilon = 1.33 \times 10^{-4}$.

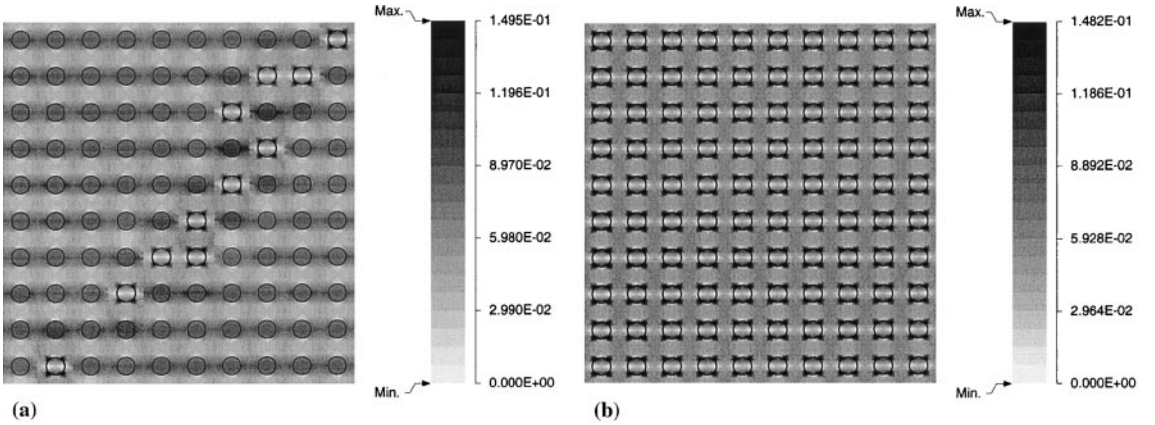

Fig. 22. Contour plots of the microscopic axial stress σ_{xx} for the uniformly dispersed microstructure (vf = 20%) at $\epsilon = 1.34 \times 10^{-4}$: (a) without periodicity and (b) with periodicity.

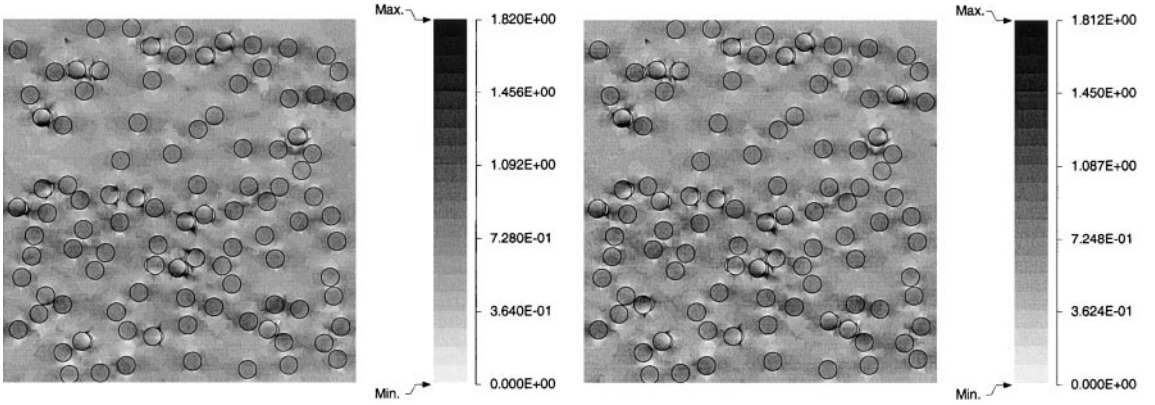

Fig. 23. Contour plots of the microscopic axial stress σ_{xx} for the randomly dispersed microstructure (vf = 20%) at $\epsilon = 1.12 \times 10^{-4}$: (a) without periodicity and (b) with periodicity.

at the poles along to the loading axis (i.e. $\theta = 0°, 180°$). This causes the fiber 2 to debond first. Following this, the radial stress in fiber 3 exceeds that of others at the poles and hence debonds. This pattern is observed for the entire load cycle. Finally, all fibers debond at higher values of the applied strain. In contrast, all fibers debond simultaneously for the periodic boundary conditions, with no apparent dominant path. A single unit cell with these periodic boundary conditions also produces identical results. It is clear from this example, that even though the microstructure may have geometric periodicity, the evolution of damage to cause failure is likely to follow a non-periodic and dominant local path. This makes the application of the conventional unit cell analysis inappropriate.

For the random microstructure, the difference in debond initiation and growth behavior with different boundary conditions is not as prominent. In contrast, the effect of local morphology is much more dominant. This is observed in Figs. 20(b) and 22. Debonding initiates in fibers that are in close proximity with other fibers and evolves randomly with increased straining. The relation between damage evolution and the local dispersion for the random microstructure is better understood from the histograms of Figs. 24 and 25. In these histograms, the relative spacing and proximity among fibers is characterized by two spatial

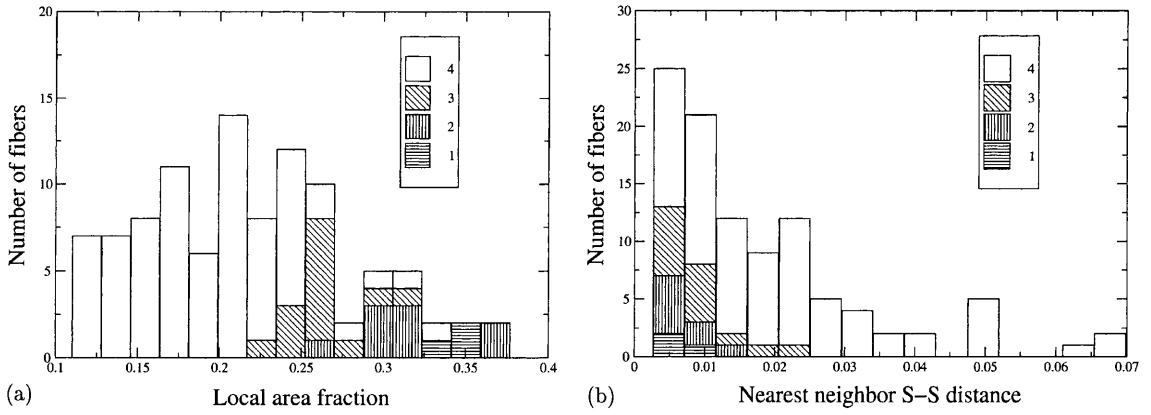

Fig. 24. Histograms showing the number of debonded and bonded fibers with increasing strain as functions of (a) local area fraction (LAF), (b) nearest neighbor surface to surface distance (NND), with periodicity boundary conditions. The strains for which these are plotted are: (1) $\epsilon = 0.96 \times 10^{-4}$, (2) $\epsilon = 1.04 \times 10^{-4}$, (3) $\epsilon = 1.12 \times 10^{-4}$. The unfilled block in (4) corresponds to the fibers with perfect interface.

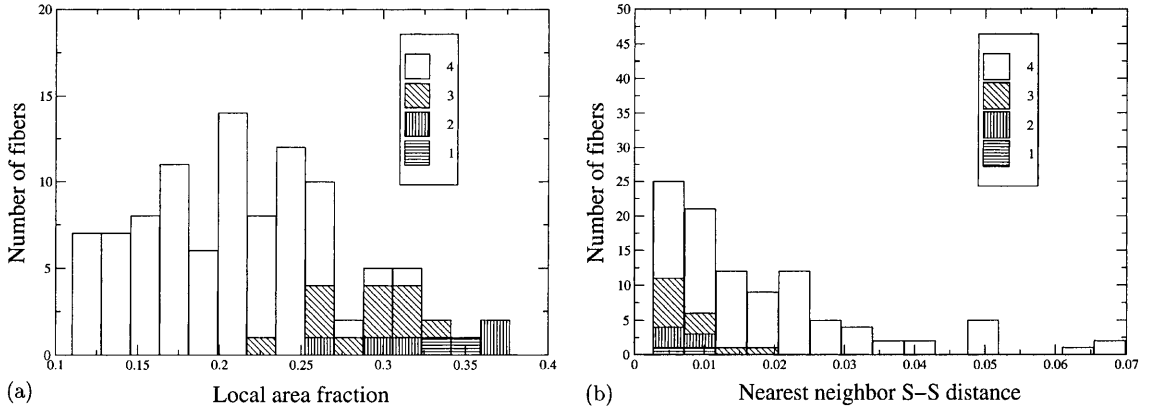

Fig. 25. Histograms showing the number of debonded and bonded fibers with increasing strain as functions of (a) local area fraction (LAF), (b) nearest neighbor surface to surface distance (NND), with displacement boundary conditions. The strains for which these are plotted are: (1) $\epsilon = 0.96 \times 10^{-4}$, (2) $\epsilon = 1.04 \times 10^{-4}$, (3) $\epsilon = 1.12 \times 10^{-4}$. The unfilled block in (4) corresponds to the fibers with perfect interface.

functions, viz. (a) local area fraction (LAF) and (b) the nearest neighbor distance (NND). The LAF is measured as the ratio of the fiber area to the area of the Voronoi cell containing it. The NND is measured as the smallest surface to surface distance between neighbors that share common Voronoi cell edges. The ordinate of the histograms represents the total number, as well as the number of debonded fibers as functions of the characterization functions LAF and NND. Different shades are used to delineate additionally debonded fibers with increasing strain. The LAF function has a bell shaped distribution whereas the NND function is clearly monotonically decreasing for the total number (debonded + intact) fibers. Debonding initiates at the higher values of LAF and lower values of NND. There is a monotonic decrease of debonded fibers with decreasing LAF and increasing NND. The monotonicity is particularly obvious for the latter function. The low NND represents closely packed fibers which are more likely to debond early in

Table 4
The relation between quantitative descriptors of the microstructure and the damage propagation for displacement (Di) and periodic (Pe) boundary conditions. Values of strain should be read as $\epsilon \times 10^{-4}$. D stands for debonded and B is for bonded at a particular strain

Fiber #	LAF%	NND (mm)	$\epsilon = 0.96$		$\epsilon = 1.04$		$\epsilon = 1.12$	
			Di	Pe	Di	Pe	Di	Pe
1	34.26	0.819	D	D	D	D	D	D
2	25.75	2.388	B	B	D	D	D	D
3	25.76	0.916	B	B	B	D	D	D
4	25.12	1.336	B	B	B	B	D	D
5	21.30	2.390	B	B	B	B	B	D
6	11.01	6.453	B	B	B	B	B	B

the loading cycle. Similar responses are obtained for both periodic and displacement boundary conditions. The statistics of debonding are also tabulated in Table 4.

The effect of volume or area fractions are also investigated through a second area fraction of $v_f = 10\%$. Both constant and randomly varying sizes of randomly dispersed fibers are considered for the 10% microstructure. The macroscopic responses for these models are plotted in Fig. 20. As long as the volume fraction is the same, the overall stiffness is not very sensitive to the size distribution, i.e., it is quite close for both the constant and the randomly varying diameters. However, the dependence of damage on the size distribution is considerable and occurs earlier for the variable size. The onset of debonding is considerably delayed for the lower volume fraction, due to increased average spacing between fibers which result in lower stress concentration. In summary, the process of initiation and growth of damage by interfacial debonding depends on several competing factors such as morphology, fiber interaction, load and boundary conditions. It is important to include large portions of the microstructure to capture the different effects. This is a shortcoming of the unit cell analyses.

4. Concluding remarks

The initiation and growth of damage by interfacial decohesion in multiple-fiber polymer matrix composites is analyzed with in-plane loading in this paper. The fiber and matrix phases are modeled with elastic properties. The progress of interfacial debonding with quasi-static loading is modeled by cohesive zone constitutive relations in terms of normal and tangential tractions and interfacial separation. In these relations, the traction increases with separation reaches a maximum and subsequently subsides to zero traction, signaling debonding. The stress and damage analyses are conducted with the Voronoi cell finite element model, that has been established as an effective tool for modeling of non-uniform microstructures. VCFEM has been developed (see Moorthy and Ghosh, 1996, 2000) to yield high computational efficiency with good accuracy for modeling large heterogeneous microstructures.

The VCFE model for interfacial debonding has been compared with a variety of established results in literature, details of which are reported in the M.S. thesis of Ling (2000). A combined experimental-computational study is conducted for specimens of polymer matrix composites in this paper. An inverse methodology, based on minimizing the difference in the macroscopic stress–strain plots, is developed for calibrating the cohesive model parameters from simple experimental results. Single and multiple fiber cruciforms specimens of circular and elliptical shapes are fabricated to avoid stress concentrations. VCFE debonding analyses are conducted to simulate experiments with other specimens. The microscopic debonding angle in experiments is estimated by a dye penetration technique. Good agreement is obtained between experiments and the simulations, both with respect to macroscopic (averaged stress–strain behavior) and microscopic (debond angle) observations.

In numerical simulations of multiple fibers microstructures, different morphologies and boundary conditions are analyzed to understand their influence on the decohesion process. Different architectures include uniform and random dispersions, different volume fractions and different size distributions. The boundary conditions include periodicity and displacement conditions. For the uniform microstructure, the path of growing damage is found to be very sensitive to the boundary conditions. Even with periodic geometric features, a distinct non-periodic and dominant damage path evolves with increasing strain, for non-periodic boundary conditions. This effect is significant at higher volume fractions. Periodic damage is only observed with periodic conditions. Such behavior make unit cell analysis with periodic boundary conditions, inadequate. For random microstructures, the debond induced damage is found to be more sensitive to the local morphology e.g. inter-fiber spacing than to the boundary conditions. The damage growth process is observed to take place gradually over a longer range of increasing strain for the random microstructures.

This study reveals the significance of analyzing large regions of the microstructure and proves the effectiveness of the VCFEM analysis for the same. The Voronoi cells also play an important role in developing geometric descriptors for quantitative characterization (e.g. LAF, NND) since they represent regions of immediate influence for each fiber and also delineate neighbors. It provides the essential link between the microstructural features and response, that is important in damage analysis.

Acknowledgements

The authors would like to gratefully acknowledge the help of Dr. N.J. Pagano for his valuable advice. This work has been supported by the Air Force Office of Scientific Research through grant No. F49620-98-1-01-93 (Program Director: Dr. T. Hahn). This sponsorship is gratefully acknowledged. Computer support by the Ohio Supercomputer Center through grant #PAS813-2 is also gratefully acknowledged.

References

Achenbach, J.D., Zhu, H., 1990. Effect of interphases on micro and macromechanical behavior of hexagonal-array fiber composites. J. Appl. Mech. 57, 956–963.

Allen, D.H., Jones, R.H., Boyd, J.G., 1994. Micro-mechanical analysis of continuous fiber metal matrix composite including the effects of matrix visco-plasticity and evolving damage. J. Mech. Phys. Solids 42, 502–529.

Barenblatt, G.I., 1962. The mathematical theory of equilibrium of cracks in brittle fracture. Adv. Appl. Mech. 7, 55–129.

Benveniste, Y., 1984. On the effect of debonding on the overall behavior of composite materials. Mech. Mater. 3, 349–358.

Camacho, G.T., Ortiz, M., 1996. Computational modelling of impact damage in brittle materials. Int. J. Solids Struct. 33 (20–22), 2899–2938.

Costanzo, F., Allen, D.H., 1995. A continuum thermodynamic analysis of cohesive zone models. Int. J. Engrg. Sci. 33, 2197–2219.

Costanzo, F., Walton, J.R., 1997. A study of dynamic crack growth in elastic materials using a cohesive zone model. Int. J. Engrg. Sci. 35, 1085–1114.

Dugdale, D.S., 1960. Yielding of steel sheets containing clits. J. Mech. Phys. Solids 8, 100–104.

Geubelle, P.H., 1995. Finite deformation effects in homogeneous and interfacial fracture. Int. J. Solids Struct. 32, 1003–1016.

Ghosh, S., Moorthy, S., 1995. Elastic–plastic analysis of arbitrary heterogeneous materials with the Voronoi cell finite element method. Comput. Meth. Appl. Mech. Engrg 121, 373–409.

Ghosh, S., Mukhopadhyay, S.N., 1991. A two dimensional automatic mesh generator for finite element analysis of randomly dispersed composites. Comput. Struct. 41, 245–256.

Gundel, D.B., Majumdar, B.S., Miracle, D.B., 1995. Evaluation of the intrinsic transverse response of fiber reinforced composites using a cross-shaped sample geometry. Scripta Metall. 33, 2057.

Hashin, Z., 1990. Thermoelastic properties of fiber composites with imperfect interface. Mech. Mater. 8, 333–348.

Li, M., Ghosh, S., Richmond, O., Weiland, H., Rouns, T.N., 1999. Three dimensional characterization and modeling of particle reinforced metal matrix composites: Part I, Quantitative description of microstructural morphology. Mater. Sci. Engrg. A 265, 153–173.

Lin, G., Geubelle, P.H., Scottos, N.R., in press. Simulation of fiber debonding and frictional sliding in a model composite pushout test. Int. J. Solids Struct. (in press).

Ling, Y., 2000. Development of the Voronoi cell finite element model for interfacial debonding in elastic composites, M.S. thesis. The Ohio State University.

Lissenden, C.J., 1990. Fiber-matrix interfacial constitutive relations for metal-matrix composites. Composites B 30, 267–278.

Lo, D.C., Allen, D.H., 1994. Modeling of delamination damage evolution on laminated composites subjected to low velocity impact. Int. J. Damage 3, 378–407.

Majumdar, B.S., Gundel, D.B., Dutton, R., Warrier, S.G., Pagano, N.J., 1998. Evaluation of the tensile interface strength in brittle matrix composite systems. J. Am. Ceram. Soc. 81 (6), 1600–1610.

Moorthy, S., Ghosh, S., 1996. A model for analysis of arbitrary composite and porous microstructures with Voronoi cell finite elements. Int. J. Numer. Meth. Engrg. 39, 2363–2398.

Moorthy, S., Ghosh, S., 2000. Adaptivity and convergence in the Voronoi cell finite element model for analyzing heterogeneous materials. Comput Meth Appl Mech Engrg. 185, 37–74.

Muskhelishvili, N.I., 1961. Some basic problems in the mathematical theory of elasticity. P. Nordhoff Ltd.

Needleman, A., 1987. A continuum model for void nucleation by inclusion debonding. J. Appl. Mech. 54, 525–531.

Needleman, A., 1990. An analysis of decohesion along an imperfect interface. Int. J. Fracture 42, 21–40.

Needleman, A., 1992. Micromechanical modeling of interfacial decohesion. Ultramicroscopy 40, 203–214.

Ortiz, M., Pandolfi, A., 1999. finite-deformation irreversible cohesive element for three-dimensional crack-propagation analysis. Int. J. Numer. Meth. Engrg. 44, 1267–1282.

Pagano, N.J., Tandon, G.P., 1990. Modeling of imperfect bonding in fiber reinforced brittle matrix composites. Mech. Mater. 9, 49–64.

Rice, J.R., 1968. Mathematical analysis in the mechanics of fracture. In: Liebowitz, H. (Ed.), Fracture. Academic Press, New York, pp. 191–311.

Tandon, R., Kim, R., Warrier, S.G., Majumdar, B.S., 1998. Influence of edge effects in estimating interfacial normal strength in model unidirectional composites. Composites B 30, 115–134.

Tvergaard, V., 1995. Fiber debonding and breakage in a whisker reinforced metal. Mater. Sci. Engrg. A 190, 215–222.

Tvergaard, V., 1990. Effect of fiber debonding in a whisker-reinforced metal. Mater. Sci. Engrg. A 125, 203–213.

Ungsuwarungsri, T., Knauss, W.G., 1987. The role of damage-softened material behavior in the fracture of composites and adhesives. Int. J. Fracture 35, 221–241.

Walter, M.E., Ravichandran, G., Ortiz, M., 1997. Computational modeling of damage evolution in unidirectional fiber-reinforced ceramic-matrix composites. Comput. Mech. 20 (1–2), 192–198.

Zhong, X.A., Knauss, W.G., 1997. Analysis of interfacial failure in particle filled elastomers. J. Engrg. Mater. Tech. 119 (3), 198–204.